Error-Detectable Bosonic Entangling Gates with a Noisy Ancilla

Takahiro Tsunoda,[1,2,*,§] James D. Teoh,[1,2,†,§] William D. Kalfus,[1,2] Stijn J. de Graaf,[1,2] Benjamin J. Chapman,[1,2] Jacob C. Curtis,[1,2] Neel Thakur,[1,2] Steven M. Girvin,[1,2] and Robert J. Schoelkopf[1,2,‡]

[1] *Departments of Applied Physics and Physics, Yale University, New Haven, Connecticut, USA*
[2] *Yale Quantum Institute, Yale University, New Haven, Connecticut, USA*

(Received 23 December 2022; revised 26 April 2023; accepted 8 May 2023; published 28 June 2023)

Bosonic quantum error correction has proven to be a successful approach for extending the coherence of quantum memories, but to execute deep quantum circuits, high-fidelity gates between encoded qubits are needed. To that end, we present a family of error-detectable two-qubit gates for a variety of bosonic encodings. From a new geometric framework based on a "Bloch sphere" of bosonic operators, we construct $ZZ_L(\theta)$ and exponential-SWAP(θ) gates for the binomial, four-legged cat, dual-rail, and several other bosonic codes. The gate Hamiltonian is simple to engineer, requiring only a programmable beam splitter between two bosonic qubits and an ancilla dispersively coupled to one qubit. This Hamiltonian can be realized in circuit QED hardware with ancilla transmons and microwave cavities. The proposed theoretical framework was developed for circuit QED but is generalizable to any platform that can effectively generate this Hamiltonian. Crucially, one can also detect first-order errors in the ancilla and the bosonic qubits during the gates. We show that this allows one to reach error-detected gate fidelities at the 0.01% level with today's hardware, limited only by second-order hardware errors.

DOI: 10.1103/PRXQuantum.4.020354

I. INTRODUCTION

High-fidelity two-qubit entangling gates are crucial for implementing useful quantum circuits. For the most part, efforts to enhance two-qubit gate performance have focused on hardware-level improvements that increase qubit coherence lifetimes [1–4], T_{coh}, and decrease gate duration τ_{gate}, while also minimizing unwanted crosstalk [5–10]. The success in engineering ever-lower physical gate errors, $p_{\text{phys}} \propto \tau_{\text{gate}}/T_{\text{coh}}$, has enabled two-qubit gate fidelities in excess of 99% in many-qubit processors using trapped ions and superconducting qubits [11–16]. But beyond these hardware-level improvements, are there other resources we can exploit?

Here we explore gates that have error-detection built in at the hardware level. In systems with both high-fidelity readout and more than two energy levels [17], we may boost the gate fidelity by engineering a scheme in which extra levels in an ancilla act as flag states for dominant errors [18–21]. Errors are detected in these gates with probability $p_{\text{fail}} \propto p_{\text{phys}}$. However, for gates where no errors are detected, the gate infidelity, $\varepsilon_{\text{pass}}$, scales in proportion to $p_{\text{phys}}{}^2$ by requiring two hardware errors during the gate to avoid detection. This quadratic scaling—rather than linear scaling—amplifies the benefits of further decreasing p_{phys}.

As shown in Fig. 1, detecting errors is useful in several important contexts, even when we do not immediately correct them at the gate level. For example, in any stabilizer code, such as the surface code, a detected error can be treated as an erasure error on a particular qubit [19–21]. For circuits in which erasures dominate over Pauli errors, the fault-tolerance threshold is substantially higher, thereby reducing the hardware requirements. Meanwhile, in noisy intermediate-scale quantum algorithms with shallow-depth circuits, simply postselecting shots in which no errors were detected is a viable strategy [22].

In this paper, we show how a circuit QED (cQED) system [23,24] can implement any excitation-preserving logical two-qubit gate for a wide range of bosonic encodings, including binomial codes [25], cat codes [26,27], rotationally symmetric codes [28], and the dual-rail code [29,30], while detecting the dominant ancilla decay and

*takahiro.tsunoda@yale.edu
†james.teoh@yale.edu
‡robert.schoelkopf@yale.edu
§These authors contributed equally to this work.

Published by the American Physical Society under the terms of the Creative Commons Attribution 4.0 International license. Further distribution of this work must maintain attribution to the author(s) and the published article's title, journal citation, and DOI.

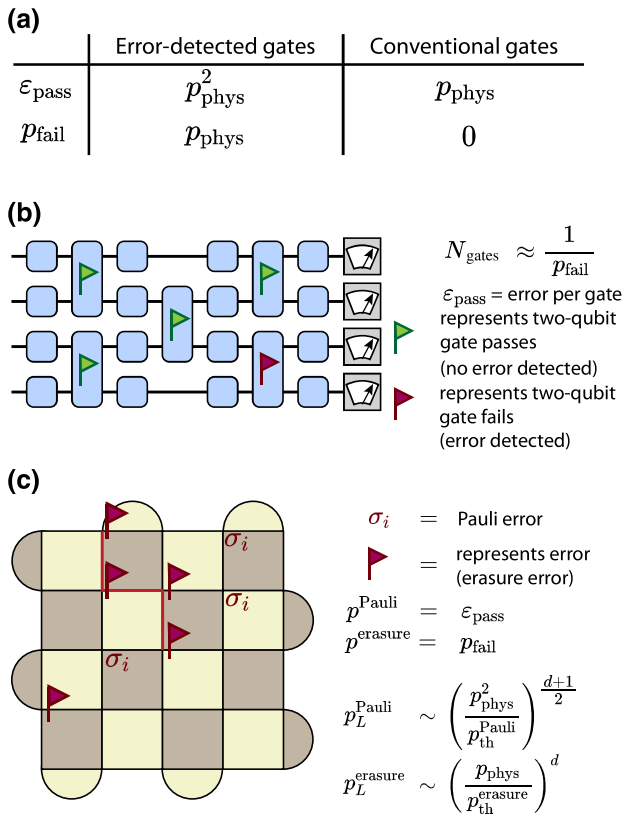

FIG. 1. Overview of how error-detected gates are useful for quantum computing tasks. (a) Unlike conventional gates, error-detected gates can be characterized by p_{fail}, the probability an error is detected during the gate, and $\varepsilon_{\text{pass}}$, the average gate error when no errors are detected. By carefully constructing the Hamiltonians that realize the gates, we can detect the dominant hardware errors, such as relaxation and dephasing events to first order (approximately p_{phys}), while two or more hardware errors are undetectable and contribute to $\varepsilon_{\text{pass}} \sim p_{\text{phys}}^2$. When gates are coherence limited, $\varepsilon_{\text{pass}}$ can be orders of magnitude smaller than p_{fail}. In contrast, conventional gates without error detection have $\varepsilon_{\text{pass}} = p_{\text{phys}}$, and $p_{\text{fail}} = 0$. (b) Noisy intermediate-scale quantum uses for error-detected gates. By postselecting short depth circuits for experiment runs where no gate errors are detected, we can effectively reach gate fidelities limited by p_{phys}^2 rather than just p_{phys}. The overall success probability exponentially decreases with circuit depth, limiting our total number of gates N_{gates} to roughly $1/p_{\text{fail}}$. (c) With real-time feedback and fast qubit reset, detected gate errors can be converted into erasure errors on data qubits in a fully-error-correcting code. For any stabilizer code [35], we can effectively double the code distance, d, by using error-detected gates. Here we use the surface code as an example, where we see p_L^{erasure} and p_L^{Pauli}, the two contributions to the total logical error rate due to erasure and Pauli errors respectively, both scale as $(p_{\text{phys}})^d$ rather than $(p_{\text{phys}})^{d/2}$. Error-detected gates also make it easier to reach below-threshold gate errors since we should compare $p^{\text{Pauli}} \sim p_{\text{phys}}^2$ with the Pauli error threshold, $p_{\text{th}}^{\text{Pauli}}$, and $p^{\text{erasure}} \sim p_{\text{phys}}$ with the erasure threshold, $p_{\text{th}}^{\text{erasure}}$, which is around a factor of 5 larger than $p_{\text{th}}^{\text{Pauli}}$ for the surface code [18].

dephasing errors. Surprisingly, this can be realized with only a programmable beam splitter interaction between two bosonic modes plus a single three-level ancilla dispersively coupled to one of these modes [31]. We develop a powerful geometric framework to represent the oscillator dynamics under this Hamiltonian on a Bloch sphere, enabling the straightforward design of two-qubit gates on bosonic modes, while also providing a natural means for incorporating ancilla error detection. Building on previous work on fault-tolerant single-qubit gates for bosonic codes [32,33], we use the $|e\rangle$ and $|f\rangle$ levels of the three-level ancilla as flag states for all first-order ancilla errors during two-qubit gates, such as single phase flip errors or decay errors.

To demonstrate the power of this protocol, we simulate the performance of logical two-qubit gates on binomial and dual-rail encoded qubits. With typical hardware parameters and error rates, we find an expected gate infidelity below 0.01% and verify $\varepsilon_{\text{pass}} \propto p_{\text{phys}}^2$. This offers a 2 orders of magnitude improvement over current state-of-the-art gate infidelities in non-error-detected bosonic two-qubit gates. As expected, we also find $p_{\text{fail}} \sim 1\%$.

II. OVERVIEW OF BOSONIC TWO-QUBIT GATE DESIGN

All proposed entangling gates are based on a simple Hamiltonian, from which we can design an entire family of logical entangling gates for a variety of bosonic encodings. This Hamiltonian combines a beam splitter interaction between bosonic modes with a dispersive interaction between an ancilla and one of the modes, as shown in Fig. 2(a). It is written as

$$\widehat{\mathcal{H}}_{\chi\text{BS}} = \widehat{\mathcal{H}}_{\chi} + \widehat{\mathcal{H}}_{\text{BS}}, \tag{1}$$

where

$$\widehat{\mathcal{H}}_{\chi}/\hbar = -\frac{\chi}{2}\hat{\sigma}_z\hat{a}^\dagger\hat{a}, \tag{2}$$

$$\widehat{\mathcal{H}}_{\text{BS}}/\hbar = \frac{g(t)}{2}\left(e^{i\varphi(t)}\hat{a}^\dagger\hat{b} + e^{-i\varphi(t)}\hat{a}\hat{b}^\dagger\right) + \Delta(t)\hat{a}^\dagger\hat{a}, \tag{3}$$

and $\hat{\sigma}_z \equiv |g\rangle\langle g| - |f\rangle\langle f|$ is the Pauli Z operator in the two-level subspace defined by the $|g\rangle$ and $|f\rangle$ levels of the ancilla. A three-level ancilla is used solely because it allows us to reserve the $|e\rangle$ level for detection of a single ancilla decay event [33,34]. The annihilation operators $\hat{a}$ and $\hat{b}$ act on the two bosonic modes, g is the strength of the beam splitter interaction, Δ is an effective detuning between two modes, and χ is the strength of the dispersive interaction between the ancilla (in the g-f manifold) and mode $\hat{a}$. We have written this Hamiltonian in a frame where the dispersive interaction is symmetric, shifting the frequency of $\hat{a}$ by $\pm\chi/2$ dependent on the ancilla state.

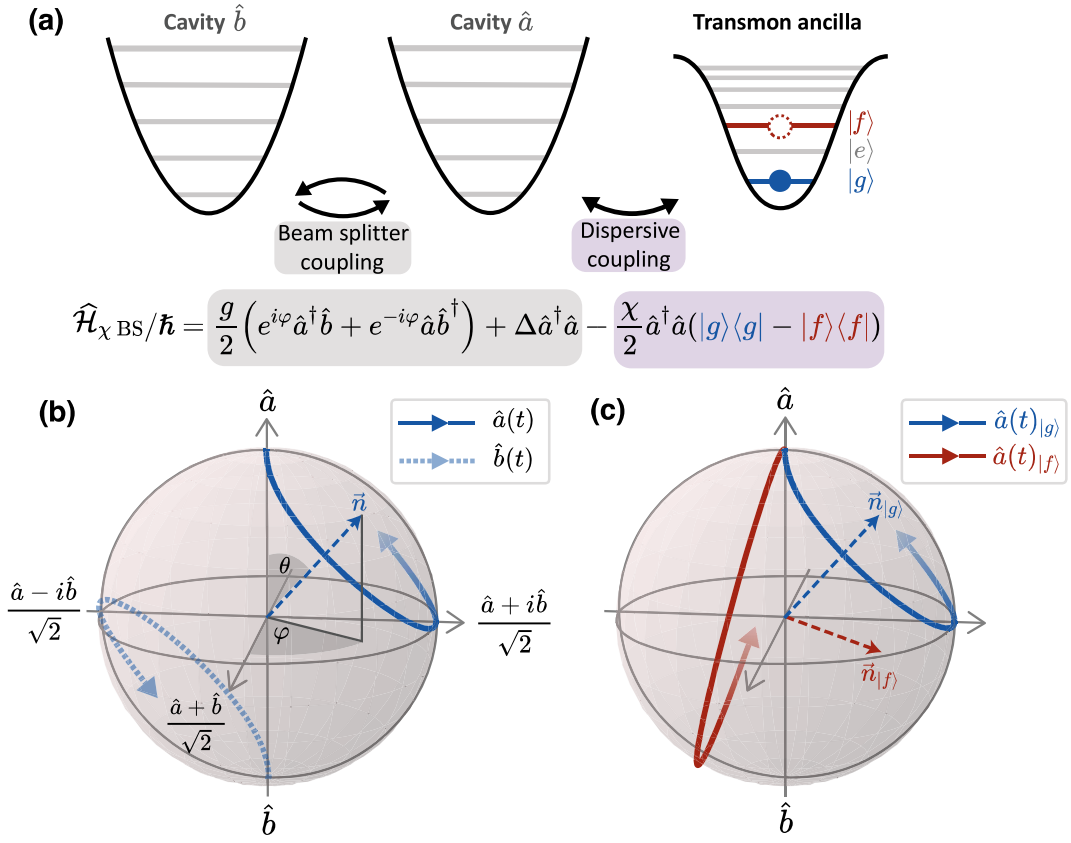

FIG. 2. Operator Bloch sphere framework for designing entangling gates for bosonic qubits. (a) Physical system and Hamiltonian $\hat{\mathcal{H}}_{\chi\mathrm{BS}}$ used to generate the gates. Two bosonic modes are coupled by a programmable beam splitter interaction (gray). Simultaneously, one of the modes is dispersively coupled (purple) to an ancilla, which may be a transmon. We operate the transmon in the g-f manifold, reserving the $|e\rangle$ state for error detection of a single ancilla decay event. (b) Application of the beam splitter interaction causes the bosonic operators to evolve in time in the Heisenberg picture. The new modes are linear combinations of the original mode operators $\hat{a}$ and $\hat{b}$, and this time evolution can be represented geometrically by the trajectories shown in blue. Trajectories orbit the precession vector $\vec{n}$, which is fully determined by Hamiltonian parameters: g and Δ set the polar angle, θ, whereas φ sets the azimuthal angle. (c) When an ancilla is dispersively coupled to one of the bosonic modes, the precession vector $\vec{n}$ becomes dependent on the ancilla state, yielding distinct vectors $\vec{n}_g$ and $\vec{n}_f$. Furthermore, if the ancilla is in a superposition of $|g\rangle$ and $|f\rangle$, the bosonic modes will be in a superposition of the two trajectories shown in the figure. The $\hat{b}(t)$ trajectories are antipodal to the $\hat{a}(t)$ trajectories and are not shown on this Bloch sphere.

Such a Hamiltonian, $\hat{\mathcal{H}}_\chi$, is routinely engineered in cQED systems [23,36,37], where superconducting cavities serve as bosonic storage modes and a transmon is used as an ancilla. The dispersive interaction was commonly used as the source of nonlinearity in previous implementations of two-qubit entangling gates with bosonic qubits in circuit QED [31,38,39] and limits gate speeds to approximately $1/\chi$, typically 1 μs. Gate fidelities were also limited by transmon decoherence ($T_{\mathrm{coh}} \sim 10$–100 μs), which sets $p_{\mathrm{phys}} \sim 1$–10%.

The gates we introduce also rely on the dispersive interaction and similar coherence times, giving comparable gate speeds and p_{phys}. However, by designing our gates to be error-detectable, we can in principle reduce remaining gate infidelity by 2 orders of magnitude with today's coherence times at the cost of gate failure probability p_{fail}. Figure 1 shows how this error-detection capability is a useful resource both in the short term (where it can boost fidelities via postselection) and in the long term (where we can treat detected errors as erasure errors to improve performance of error-correcting codes).

The second term, $\hat{\mathcal{H}}_{\mathrm{BS}}$, represents the beam splitter interaction between two cavities that can be generated by a driven nonlinear coupling element, such as a transmon [31,40], superconducting nonlinear asymmetric inductive element [41,42], or superconducting quantum interference device [43,44]. Since this parametric interaction may be actuated by one or more microwave drive signals, many of the parameters in the Hamiltonian, such as the coupling strength g, its phase φ, and its detuning Δ, can be rapidly and easily varied via standard microwave techniques. Thus, we can exploit the full time-dependent control of

g, φ, and Δ to engineer new operations, even though the strength of the dispersive interaction χ is usually fixed. We assume that actuating the beam splitter Hamiltonian does not introduce any new significant sources of error into our system [41,43].

Although an ancilla couples to only one of the bosonic modes, in the presence of a beam splitter interaction both modes interact with the ancilla, thereby enabling various nontrivial two-mode operations. The large size of the joint Hilbert space, however, can make the dynamics of this Hamiltonian difficult to interpret. In general, this Hamiltonian can drive logical states out of the codespace. A simple example is the Hong-Ou-Mandel effect, which can take two qubits encoded in the "Fock 0-1" encoding ($|0_L\rangle = |0\rangle, |1_L\rangle = |1\rangle$) to superpositions of $|0\rangle$ and $|2\rangle$ when we start in the state $|1_L 1_L\rangle$. This is different from typical implementations for two-level qubits [5,6,45], where logical states remain in the two-qubit subspace throughout the gate.

We show that this complexity can be handled by mapping the dynamics to an "operator Bloch sphere" in Sec. III. In Sec. IV we identify useful unitaries generated by $\widehat{\mathcal{H}}_{\chi\mathrm{BS}}$—namely, the ancilla-controlled ZZ_L, cZZ_L, and ancilla-controlled SWAP, cSWAP, unitaries. In Sec. V, we interleave the ancilla-controlled unitaries with ancilla rotations to turn these into parameterized $ZZ_L(\theta)$ and exponential-SWAP(θ) [eSWAP(θ)] logical gates. Combining these with existing $Z_L(\theta)$ gates allows us to realize any excitation-preserving two-qubit logical gate (see Appendix F). In Sec. VI we describe how these gate constructions also allow us to detect errors in the ancilla and preserve the error-detection properties of the bosonic encodings. Finally, in Sec. VII we show in simulations that we can achieve error-detected two-qubit gate infidelities $\varepsilon_{\mathrm{pass}} \propto p_{\mathrm{phys}}^2 \sim 0.01\%$ with reasonable hardware coherence times and a failure rate $p_{\mathrm{fail}} \propto p_{\mathrm{phys}} \sim 1\%$.

III. OPERATOR BLOCH SPHERE FRAMEWORK FOR BEAM SPLITTER INTERACTIONS

We introduce the "operator Bloch sphere" to visualize the dynamics generated by $\widehat{\mathcal{H}}_{\chi\mathrm{BS}}$ and port existing intuition for single-qubit control on the Bloch sphere to the design of two-qubit gates for bosonic qubits. Working in the Heisenberg picture allows us to avoid tracking the evolution of every two-mode state. To begin, we consider evolution under $\widehat{\mathcal{H}}_{\mathrm{BS}}$, then generalize to the full $\widehat{\mathcal{H}}_{\chi\mathrm{BS}}$ Hamiltonian.

Inspired by Schwinger's angular momentum formalism of bosonic operators [46], we rewrite $\widehat{\mathcal{H}}_{\mathrm{BS}}$ with the angular momentum operators $\widehat{L}_I = \frac{1}{2}(\hat{a}^\dagger\hat{a} + \hat{b}^\dagger\hat{b})$, $\widehat{L}_X = \frac{1}{2}(\hat{a}^\dagger\hat{b} + \hat{a}\hat{b}^\dagger)$, $\widehat{L}_Y = 1/2i(\hat{a}^\dagger\hat{b} - \hat{a}\hat{b}^\dagger)$, and $\widehat{L}_Z = \frac{1}{2}(\hat{a}^\dagger\hat{a} - \hat{b}^\dagger\hat{b})$, which allows us to rewrite $\widehat{\mathcal{H}}_{\mathrm{BS}}$ as

$$\widehat{\mathcal{H}}_{\mathrm{BS}}(g,\varphi,\Delta)/\hbar = g\cos\varphi\widehat{L}_X - g\sin\varphi\widehat{L}_Y + \Delta\widehat{L}_Z + \Delta\widehat{L}_I.$$

For the case where the parameters g, φ, and Δ are constant, the Heisenberg representation of the mode operators can be obtained by transforming the mode operators via the unitary operator $\widehat{U} = \exp(-i\widehat{\mathcal{H}}_{\mathrm{BS}}t/\hbar)$,

$$\begin{pmatrix}\hat{a}(t)\\ \hat{b}(t)\end{pmatrix} = \begin{pmatrix}\widehat{U}\hat{a}\widehat{U}^\dagger\\ \widehat{U}\hat{b}\widehat{U}^\dagger\end{pmatrix} = e^{-i\Delta/2t}R_{\vec{n}}(\Omega t)\begin{pmatrix}\hat{a}\\ \hat{b}\end{pmatrix}, \tag{4}$$

where $R_{\vec{n}}(\Omega t) = (\cos\Omega t/2 I - i\sin\Omega t/2\vec{n}\cdot\vec{\sigma})$ is a matrix in SU(2), which can be interpreted as a rotation around a precession vector $\vec{n} = [\sin\theta\cos\varphi, -\sin\theta\sin\varphi, \cos\theta]$ at rate $\Omega = \sqrt{g^2+\Delta^2}$ [47]. The polar angle of the precession vector is determined by the ratio of the coupling strength g and the detuning Δ such that $\cos\theta = \Delta/\sqrt{g^2+\Delta^2}$ and $\sin\theta = g/\sqrt{g^2+\Delta^2}$. Analogously to state evolution on a qubit Bloch sphere, we plot the mode transformations at each point in time to form trajectories on the operator Bloch sphere, as shown in Fig. 2(b). Here the north pole represents the initial mode operator $\hat{a}$ and the solid arrow represents the trajectory of the transformed mode operator $\hat{a}(t)$. Similarly, the south pole represents the initial mode operator $\hat{b}$ and the dashed arrow represents the trajectory of the transformed mode operator $\hat{b}(t)$. The trajectory can be fully controlled by modulating the complex amplitude of the beam splitter interaction, which is routinely done in the cQED systems [31,41,43]. The trajectories from the north pole and the south pole are antipodal to one another and therefore we show only the transformation of $\hat{a}$ going forward. The endpoints of the trajectories indicate the final mode transformations of the original $\hat{a}, \hat{b}$ operators.

The effect of the ancilla's interaction, $\widehat{\mathcal{H}}_\chi$, appears as an ancilla-state-dependent detuning $\Delta = \Delta' \pm \chi/2$, where Δ' now represents the detuning of the beam splitter drives from resonance. We can now write the dispersive beam splitter Hamiltonian as

$$\begin{aligned}\widehat{\mathcal{H}}_{\chi\mathrm{BS}} = {}& \widehat{\mathcal{H}}_{\mathrm{BS}}\left(g,\varphi,\Delta'-\frac{\chi}{2}\right)\otimes|g\rangle\langle g| \\ & + \widehat{\mathcal{H}}_{\mathrm{BS}}\left(g,\varphi,\Delta'+\frac{\chi}{2}\right)\otimes|f\rangle\langle f|.\end{aligned} \tag{5}$$

Since the total detuning of the beam splitter becomes dependent on the ancilla state, there now exist two different "conditional" precession vectors with different z components, allowing us to construct ancilla-controlled mode trajectories. This is illustrated in Fig. 2(c).

All possible dynamics generated by the detuned beam splitter Hamiltonian can be represented on the operator Bloch sphere. The three degrees of freedom in the dispersive beam splitter Hamiltonian g, φ, and Δ determine the axis and rate of precession. This holds true even when these parameters have time dependence, which leads to time-varying precession axes and precession rates. We emphasize that the operator Bloch sphere picture is necessary to visualize the time dynamics generated by a

TABLE I. Pump conditions for primitive operations. The beam splitter rate g, pump detuning Δ, and pulse duration required to perform key primitive operations (up to ancilla-state-dependent local rotations).

Hamiltonian parameter	cZZ$_L$ for Fock 0-1 or dual rail	cZZ$_L$ for binomial or four-legged cat	cSWAP
g	$\sqrt{3}/2\chi$	$\sqrt{15}/2\chi$	$\chi/\sqrt{3}$
Δ	0	0	$\chi/2$
T	$2\pi/\chi$	π/χ	$\sqrt{3}\pi/\chi$

continuous beam splitter interaction, over which we have fine control of the Hamiltonian parameters. This differs from the discrete beam splitter transformations found in linear optics [48].

IV. ANCILLA-CONTROLLED LOGICAL UNITARIES

The operator Bloch sphere picture is a powerful tool for finding new and interesting ancilla-controlled unitaries generated by $\widehat{\mathcal{H}}_{\chi\mathrm{BS}}$. Specifically, we show a way to realize both cZZ$_L$ and cSWAP unitaries in our simple proposed hardware layout.

We define ancilla-controlled unitaries as unitaries where we perform identity on the bosonic modes if the ancilla is in $|g\rangle$ and a unitary gate on the bosonic modes if the ancilla is in $|f\rangle$. At the end of the unitary, the bosonic states must return to the logical codespace. This constraint restricts us to trajectories that start and end at the poles of the operator Bloch sphere, corresponding to either SWAP or identity operations. However, there is a crucial feature: the solid angle enclosed by these trajectories determines the geometric phase imparted to the bosonic modes, and is used as a resource to enact logical operations (see Appendix C). We later use this effect to engineer the cZZ$_L$ and cSWAP unitaries, as shown in Fig. 3. Moreover, by combining these unitaries with arbitrary ancilla rotations, we can construct a family of excitation-preserving gates, such as $ZZ_L(\theta)$, imaginary-SWAP(θ) [iSWAP(θ)], and fSIM(θ_1, θ_2) gates, on the logical subspace (see Appendix F).

Designing trajectories that enclose a specific geometric phase can be used to build useful unitaries. The geometric phase is set by the term $e^{-i\Delta/2t}$ in Eq. (4). Completely enclosing a solid angle ϕ corresponds to performing the unitary $\hat{R}_\phi = e^{i\phi/2(\hat{a}^\dagger\hat{a}+\hat{b}^\dagger\hat{b})}$ on the bosonic modes. For many bosonic encodings, $e^{i\pi/n\hat{a}^\dagger\hat{a}} = Z_L$ for $n \in \mathbb{Z}$, and hence $ZZ_L = e^{i\pi/n(\hat{a}^\dagger\hat{a}+\hat{b}^\dagger\hat{b})}$. This is true for both the binomial code and the four-legged cat code as defined in Appendix B where $n = 2$. Therefore, by varying the relative strengths of the microwave-controlled Hamiltonian parameters, we can choose the enclosed geometric phase to match the ZZ_L operator for a particular

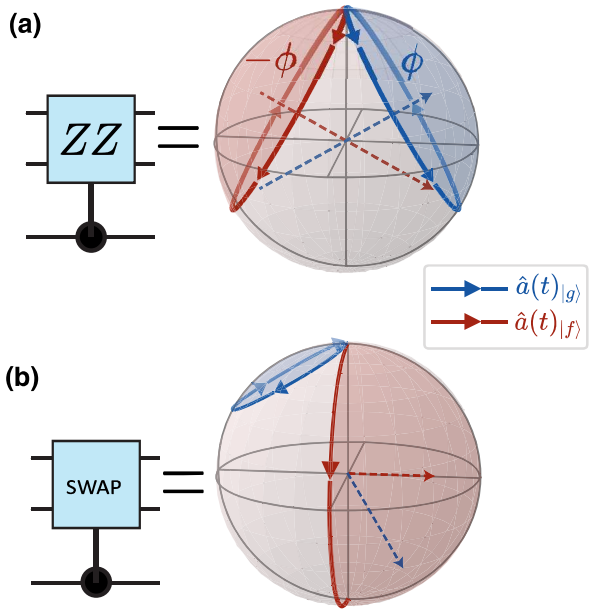

FIG. 3. cZZ and cSWAP operations on the operator Bloch sphere realized with the Hamiltonian parameters and durations listed in Table I. (a) Trajectories for the cZZ$_L$ operation. After an amount of time T, the trajectories complete a full orbit at the end of the gate and enclose area $\pm\phi$. By our choosing Hamiltonian parameters such that $\phi = \pi$, these ancilla-dependent mode transformations are equivalent to performing a cZZ unitary for the Fock 0-1 and dual-rail codes. When $\phi = \pi/2$, this is a cZZ unitary for the binomial and four-legged cat codes (see Appendix D). (b) Trajectories for the cSWAP operation. The $\hat{a}(t)_{|g\rangle}$ trajectory returns to the north pole, indicating that we perform identity on the two bosonic modes up to a geometric phase. The $\hat{a}(t)_{|f\rangle}$ trajectory ends at the south pole, which corresponds to a complete swapping of the two modes up to a geometric phase.

bosonic code. Moreover, the ability to map the system dynamics to trajectories on a Bloch sphere also allows us to import noise mitigation and gate optimization techniques developed for qubits that utilize geometric phase control [49–51].

Trajectories that depend on the two ancilla states generate three types of ancilla-controlled unitaries that return to the codespace: (a) both trajectories may return to the starting pole, (b) one trajectory returns to the starting pole, while the other returns to the opposite pole, or (c) both trajectories may return to the opposite pole. Although these trajectories are a small subset of all possible trajectories we could engineer, each case represents a different, useful ancilla-controlled logical operation.

First, we consider evolution where the two trajectories conditioned on the ancilla state return to their starting poles [Fig. 3(a)]. The geometric phase accumulation means we perform the ancilla-controlled unitary

$$e^{+i\phi/2(\hat{a}^\dagger\hat{a}+\hat{b}^\dagger\hat{b})} \otimes |g\rangle\langle g| + e^{-i\phi/2(\hat{a}^\dagger\hat{a}+\hat{b}^\dagger\hat{b})} \otimes |f\rangle\langle f|. \quad (6)$$

We can use this geometric phase accumulation to perform logical operations on the bosonic modes. For many bosonic encodings, Z_L takes the form $e^{i\pi/n a^\dagger a}$ for a code with n-fold rotational symmetry [28], and hence $ZZ_L = e^{i\pi/n(\hat{a}^\dagger\hat{a}+\hat{b}^\dagger\hat{b})}$.

When $\phi = \pi/n$ or $\phi = 2\pi(1-1/2n)$, this is equivalent to the $\mathbf{cZZ}_L$ unitary

$$\hat{\mathbb{1}} \otimes |g\rangle\langle g| + ZZ_L \otimes |f\rangle\langle f| \tag{7}$$

up to the rotation operator $e^{-i\pi/2n(\hat{a}^\dagger\hat{a}+\hat{b}^\dagger\hat{b})}$, which is easily tracked in software. The required Hamiltonian parameters are found from the general formula for the solid angle, ϕ. For orbits about a fixed precession vector, this is given by $\phi = 2\pi(1-\cos\theta) = 2\pi(1-\chi/2\Omega)$. The parameters for the cZZ_L gate are shown in Table I for bosonic codes where $Z_L = e^{i\pi\hat{a}^\dagger\hat{a}}$ or $Z_L = e^{i\pi/2\hat{a}^\dagger\hat{a}}$. Since the interaction strengths $g/2\pi$ and $\chi/2\pi$ may both be several megahertz [41,43], all these gates on multiphoton encoded qubits may be performed in times of approximately 1 μs, 3 orders of magnitude faster than typical microwave cavity decay rates (1 ms) [24], and 2 orders of magnitude faster than the transmon decoherence rate (100 μs), which yields the coherence-limited infidelity at the level of $p_{\mathrm{phys}} \propto \tau_{\mathrm{gate}}/T_{\mathrm{coh}} \sim 1$–10%, a similar scaling as for previously implemented bosonic entangling gate [31].

With another set of Hamiltonian parameters, we can create the cSWAP operation [Fig. 3(b)] defined as

$$\hat{\mathbb{1}} \otimes |g\rangle\langle g| + \mathrm{SWAP} \otimes |f\rangle\langle f|. \tag{8}$$

In this case, we need the trajectory conditioned on $|f\rangle$ to end at the opposite pole, while the trajectory conditioned on $|g\rangle$ completes an orbit about a different precession vector to return to the initial pole. For the parameters presented in Table I, this implements the unitary

$$e^{i\pi\left(1-\frac{\sqrt{3}}{2}\right)(\hat{a}^\dagger\hat{a}+\hat{b}^\dagger\hat{b})} \otimes |g\rangle\langle g| + e^{-i\pi/2(\hat{a}^\dagger\hat{a}+\hat{b}^\dagger\hat{b})} \mathrm{SWAP} \otimes |f\rangle\langle f|. \tag{9}$$

By adding appropriate delays in the gate sequence (see Appendix D), one can null unwanted geometric phase accumulations to realize the cSWAP unitary. This operation was experimentally realized in the work reported in Ref. [41].

Finally, when both trajectories end at the opposite pole, we perform a SWAP operation between the bosonic modes that is independent of the ancilla state (up to geometric phase accumulation), which we call an "unconditional SWAP (uSWAP) operation". Without use of our framework, this operation is hard to realize when the ancilla is in a superposition of states, due to the static nature of the dispersive interaction. Unconditional SWAP operations allow us to extend our ancilla-controlled unitaries that act on more than two bosonic modes (see Appendix D) .

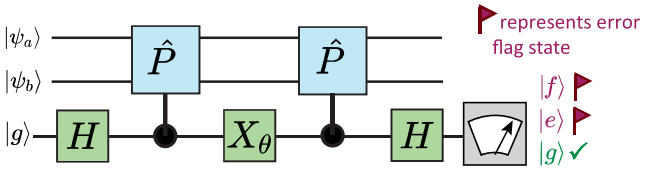

FIG. 4. Error-detected circuits for bosonic entangling gates. We interleave ancilla-controlled unitaries (in blue) with ancilla rotations in the g-f manifold (in green) to construct entangling gates. Provided $\hat{P}^2 = \hat{\mathbb{1}}$, we implement the general gate $\hat{P}(\theta) = \exp(-i\theta/2\hat{P})$. By using the cZZ_L operation introduced earlier, we execute this circuit with $\hat{P} = ZZ_L$ to perform the entangling gate $ZZ_L(\theta)$ on our bosonic qubits. Similarly, with the cSWAP operation we can perform an eSWAP(θ) entangling gate. These gates are easily parameterized via the middle X_θ ancilla rotation. Crucially, we can detect ancilla errors during the gate by measuring the state of the ancilla at the end of the circuit. Measuring the ancilla in $|e\rangle$ or $|f\rangle$ flags that an error has occurred. We accept the gate when we measure the ancilla in $|g\rangle$.

V. A FAMILY OF LOGICAL TWO-QUBIT GATES

Importantly, with just the two primitives cZZ_L and cSWAP, we can use arbitrary rotations on the ancilla to now perform a continuous family of entangling gates on the bosonic logical subspace.

Inspired by gate teleportation techniques [52–55], ancilla-controlled unitary gates on the logical subspace can be 'exponentiated' by a circuit shown in Fig. 4 [56]. The cSWAP and cZZ_L primitives by themselves are capable of generating entanglement only between the ancilla and the bosonic modes. However, with this circuit we are able to perform an entangling gate that acts only on the bosonic modes, leaving the ancilla disentangled at the end of the circuit. The ancilla should start and end in its initial state, $|g\rangle$. A key advantage of this approach is that by checking that the ancilla returns to $|g\rangle$, we can detect whether ancilla errors have occurred during the gate.

The exponentiation circuit we present is very general and allows one to realize the unitary

$$\hat{P}(\theta) = \exp\left(-i\frac{\theta}{2}\hat{P}\right) = \cos\frac{\theta}{2}\hat{I} - i\sin\frac{\theta}{2}\hat{P} \tag{10}$$

from the ancilla-controlled unitary $\mathrm{c}\hat{P}$, where $\hat{P}$ is any "Pauli-like" operator acting on the two-qubit logical subspace that satisfies $\hat{P}^2 = \hat{\mathbb{1}}$ (in other words $\hat{P}$ is Hermitian and unitary). The full unitary implemented on the qubit-ancilla system by this circuit is

$$\hat{P}(\theta) \otimes |g\rangle\langle g| + \hat{P}(-\theta) \otimes |f\rangle\langle f|. \tag{11}$$

The exponentiation circuit gives us an elegant way to control multiple logical qubits and has desirable error detection properties. One needs only to vary the angle

of the middle ancilla rotation to implement a continuous set of parameterized entangling gates, $\widehat{P}(\theta)$ on the logical qubits—the rest of the gate construction remains unchanged, making logical gates easy to calibrate for many different values of θ. The setup in Fig. 4 inherently detects a single ancilla dephasing error (see Appendix I) but not ancilla decay events, which necessitates the use of a three-level ancilla to detect these errors. Use of both error detection strategies permits us to use an ancilla that is considerably noisier than the logical qubits, since the propagation of ancilla errors to the qubits is error-detectable to first order. We explain this feature in more detail in Sec. VI.

Setting $\widehat{P} = \text{SWAP}$ with the cSWAP unitary yields a construction for the eSWAP gate [31,57]. Similarly, with the cZZ_L unitary we construct the $ZZ_L(\theta)$ gate, which has not yet been realized for bosonic qubits. An advantage of these constructions is the ease of varying the angle θ, which is controlled simply by varying the angle of the intermediate ancilla rotation in Fig. 4. For all values of θ except 0 and integer multiples of π, these gates can generate entanglement from separable input states. The gates are maximally entangling for $\theta = \pi/2$, and $ZZ_L(\pi/2)$ is equivalent to a controlled NOT gate up to single-qubit gates.

By combining eSWAP(θ) and $ZZ_L(\theta)$ gates with single-qubit $Z_L(\theta)$ gates, we can implement any excitation-preserving logical two-qubit gate on the two bosonic qubits (see Appendix F). The $Z_L(\theta)$ gate can be implemented either by use of the same construction with ancilla-controlled rotations of a single bosonic mode (which naturally arises from the dispersive interaction) or by use of a fault-tolerant selective number-dependent arbitrary phase (SNAP) gate [33,58].

The gate construction can also be used on Gottesman-Kitaev-Preskill codewords [59]. With conditional displacement Hamiltonians [60,61], one can engineer the ancilla-controlled unitaries $\text{c}Z_L$, cZZ_L, $\text{c}X_L$, $\text{c}XX_L$, etc., which, in turn, allows us to implement the gates $Z_L(\theta)$, $ZZ_L(\theta)$, $X_L(\theta)$, and $XX_L(\theta)$. In other words, we can use the construction to realize parameterized entangling gates and arbitrary single-qubit rotations in the Gottesman-Kitaev-Preskill code, while being able to detect ancilla errors during the gate. This construction resembles some of the circuits found in echoed conditional displacement control [62,63]. cQED allows the direct implementation of the required ancilla-controlled unitaries by the stringing together of conditional displacements that act on different bosonic modes coupled to the same ancilla to construct joint conditional displacements.

Another powerful application of the ancilla-controlled logical gates is to perform a quantum non-demolition (QND) logical measurement of the operator $\widehat{P}$. This is done by preparing the ancilla in $|+\rangle_{gf} \equiv (|g\rangle + |f\rangle)/\sqrt{2}$, applying $\text{c}\widehat{P}$, and then measuring the ancilla in the $|\pm\rangle_{gf}$ basis. For the cSWAP operation, this amounts to a SWAP test [41]. Similarly cZZ_L can be turned into a QND logical measurement of the ZZ_L operator. This operation finds use in measurement-based alternatives to entangling gates [64], and can form part of a Bell measurement. Unlike the gate construction, in principle these measurements can correct single ancilla decay errors and all orders of ancilla dephasing. This is explored further in Appendix H.

VI. HARDWARE EFFICIENT ERROR-DETECTED GATES

Perhaps the most exciting aspect of these gates is the ability to detect hardware errors at any time during (or before) the gates in both the ancilla and the bosonic modes. Crucially, a successful gate should always return the ancilla to $|g\rangle$. If we measure the ancilla to be in any state other than $|g\rangle$ at the end of the gate, we flag the gate as having experienced an error. Bosonic errors such as photon loss remain detectable after the gate (e.g., via photon number parity measurements). In the usual case where the ancilla has worse coherence than the bosonic modes, it is essential to prevent ancilla errors from propagating onto the bosonic modes. Otherwise, we lose the advantages of using a bosonic code in the first place.

Here we describe the critical error detection properties of the protocol for ancilla decay, ancilla dephasing, and photon loss in the bosonic modes. An in-depth discussion can be found in Appendix G 1. First, we analyze errors that occur during the ancilla-controlled unitaries, which have the longest duration in our gate sequences. The gate constructions are naturally robust with regard to ancilla dephasing but not ancilla decay. As previously mentioned, we circumvent this problem by operating the ancilla in the manifold spanned by $|g\rangle$ and $|f\rangle$, reserving the $|e\rangle$ level to detect if a single ancilla decay has occurred. This is roughly equivalent to realizing a simple noise-biased ancilla and is generalizable to ancillae in other platforms. Alternatively, two levels in a truly noise-biased ancilla [65] also suffice for implementing these circuits, provided we can prepare and measure the ancilla in the X basis and can perform bias-preserving $X(\theta)$ rotations.

Ancilla dephasing can be described by the jump operator $\hat{\sigma}_z$. Since this operator commutes with $\widehat{\mathcal{H}}_{\chi\text{BS}}$, the ancilla-controlled unitaries are error-transparent [34] to dephasing. In other words, dephasing during the unitary evolution is the same as performing the ancilla-controlled unitary correctly, and then applying the operator $\hat{\sigma}_z$ afterwards.

For the logical gate construction, we use two ancilla-controlled unitaries, and while each of these is error-transparent to dephasing, the overall circuit is not due to the ancilla rotation by angle θ in the middle. Regardless, if a dephasing jump occurs at some time during the circuit, we always read out $|f\rangle$ at the end. With no dephasing jumps, we always read out $|g\rangle$. If the jump occurs during the last ancilla-controlled unitary, the correct $ZZ_L(\theta)$ gate is performed on the bosonic modes. However, if the

jump occurs during the first control unitary, we perform a $ZZ_L(-\theta)$ operation instead. Since we cannot distinguish between the two cases, the correction unitary is unknown, and so we can only detect these errors rather than correct them.

We are also robust with regard to dephasing and decay errors that happen during the much shorter ancilla rotations. One can show that the correct gate is still performed when we measure the ancilla to be in $|g\rangle$ (see Appendix G 1). This means the error-detected gate fidelity could, in principle, exceed coherence-limited single-qubit gate fidelities found in transmon-based qubit architectures.

$\widehat{\mathcal{H}}_{\chi\mathrm{BS}}$ preserves the total photon number, and therefore photon loss during the gate remains detectable after the gate when an appropriate bosonic code is used; for example, via parity measurements [66]. Photon loss during the ancilla-controlled unitaries also dephases the ancilla, and hence only this error is detectable, just as for isolated ancilla dephasing errors.

VII. NUMERICAL SIMULATIONS of $ZZ_L(\pi/2)$ GATES

We solve the Lindblad master equation in QuTiP [68] to calculate several performance metrics for the $ZZ(\theta = \pi/2)$ gate in two bosonic codes: the lowest-order binomial code [25] and the dual-rail encoding [29]. During the simulation, the system experiences ancilla decay, ancilla dephasing, or photon loss in the bosonic modes (see Appendix J for the simulation parameters).

Our gate constructions are unable to detect intrinsic dephasing of the bosonic mode. Fortunately, in cQED, the intrinsic dephasing of a microwave cavity can be extremely small (much greater than 10 ms [34,69]), and is not modeled in our simulations. In experiment, cavity dephasing is largely caused by transmon ancilla decay at unknown times, which is error-detectable to first order and is accounted for in our simulations.

From these simulations, we obtain the average gate failure probability, p_{fail}, and the average error-detected gate infidelity, $\varepsilon_{\mathrm{pass}}$. To highlight how these metrics scale with hardware errors, we enable one error channel at a time, as shown in Fig. 5. Our proposed gates have the ability to detect all first-order jump errors associated with each error channel, and therefore only second-order jump errors limit the error-detected gate infidelity.

The numerical simulations verify this property, as shown by the quadratic scaling of $\varepsilon_{\mathrm{pass}}$ with coherence time. Values of $\varepsilon_{\mathrm{pass}}$ well below 0.01% are achieved with feasible coherence times, which would outperform any previously demonstrated two-qubit gates (errors of approximately 0.1%) in superconducting qubits [10,70] and trapped ions [4]. We also find $p_{\mathrm{fail}} \sim 1\%$, which scales linearly with hardware coherence rates.

For these simulations we choose $\chi_{gf}/2\pi = -1$ MHz, and therefore the required beam splitter rates needed for the $ZZ_L(\pi/2)$ gates are approximately 1 MHz. Hardware with the required system parameters has already been implemented [31,71], with more recent experiments demonstrating high-fidelity beam splitters with rates of up to 5 MHz [43].

We simulate the $ZZ_L(\pi/2)$ gate using the circuit in Fig. 4, with the Hamiltonian parameters listed for the cZZ_L operation in Table I for the binomial and dual-rail encoding (see Appendix A). We simplify the dynamics by choosing constant pulse profiles for the beam splitter amplitude g and for the ancilla rotation pulses, allowing us to focus on the incoherent error and ignore any coherent error associated with imperfect pulse shaping, which is thought to be negligible (see Appendix M). This also reveals that the gates are robust with regard to errors during the ancilla rotations themselves (duration 50 ns), meaning $\varepsilon_{\mathrm{pass}}$ can surpass typical transmon π-pulse coherence-limited fidelities (see Appendix I).

More realistic simulations can include higher-order nonlinearities in the Hamiltonian, which are sources of coherent errors in the gates. Nonetheless, these errors are expected to scale quadratically with gate duration. We consider the effects of self-Kerr in each cavity, cross Kerr between the cavities, and the χ' correction to the dispersive coupling in Appendix K, and show that they introduce infidelity at the 0.01% level for realistic parameters.

VIII. CONCLUSION

We introduce error-detectable two-qubit entangling gates for a wide range of bosonic qubits, including the dual-rail, binomial, and four-legged cat encodings. Our gates are based on a tunable beam splitter interaction between two bosonic modes and an ancilla dispersively coupled to just one of the modes. The time evolution during the gates can be visualized in a new geometric framework, which we call the "operator Bloch sphere". In this picture, we can easily derive the Hamiltonian parameters needed to perform ancilla-controlled unitaries cZZ_L and cSWAP. With these building blocks, we show how to construct new, fast gate implementations for the $ZZ_L(\theta)$ and $\mathrm{eSWAP}(\theta)$ gates that could be readily realized on current hardware. By using a three-level transmon as our ancilla, we are able to flag the dominant hardware errors, transmon decay, and dephasing, and prevent them from significantly impacting the gate fidelities. As a result of this strategy, we also expect quadratic improvement of the error-detected gate infidelity as we increase the hardware lifetime and the gate speed. With today's cQED hardware coherences, we expect to reach error-detected gate infidelities below 0.01% with 1% gate failure probability. We verify the quadratic scaling of these fidelities with hardware coherence times in simulations. This

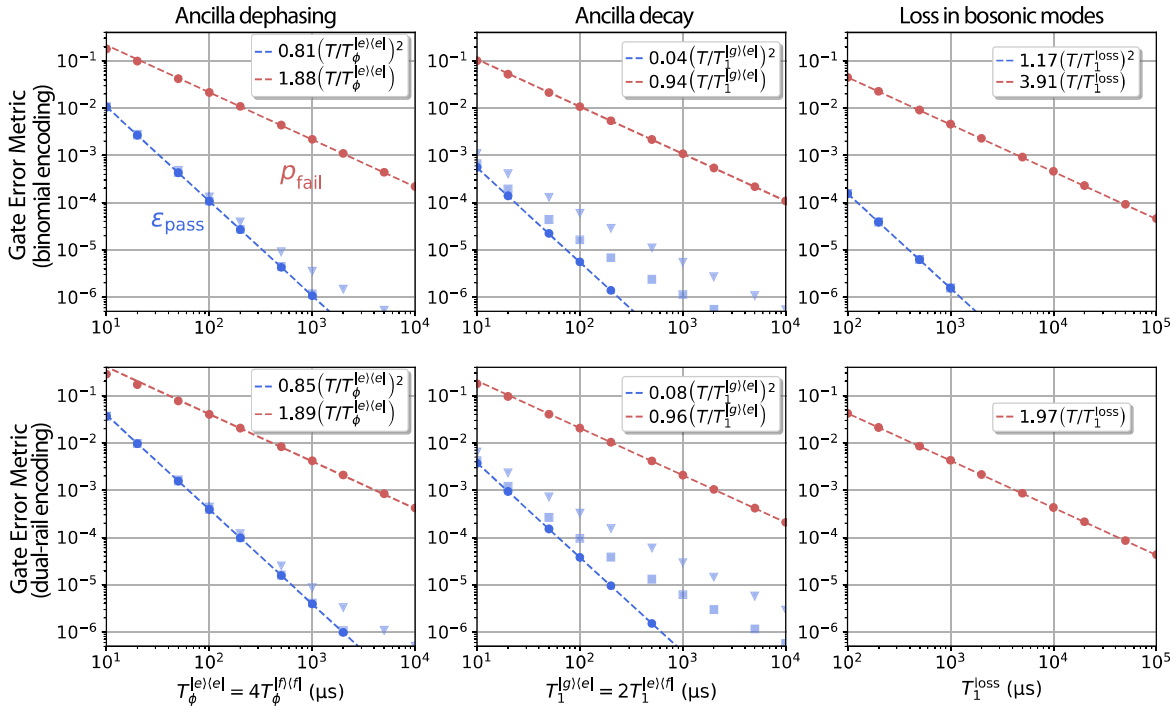

FIG. 5. Quadratic scaling of $ZZ_L(\pi/2)$ gate infidelity with hardware coherence times, reaching error-detected infidelities below 0.01%. Numerical simulation of error-detected $ZZ_L(\pi/2)$ gate on two logical qubits in both the binomial encoding (top row) and the dual-rail encoding (bottom row) under three separate error channels—ancilla decay, ancilla dephasing, and photon loss in the bosonic modes. Here we plot the average gate failure probability and average error-detected gate infidelity versus coherence time. Average gate failure probability, or p_{fail} (red circles), refers to the fraction of gate attempts where we measure the ancilla to be in $|e\rangle$ or $|f\rangle$ at the end (left and middle columns), or when we detect photon loss in the bosonic modes via idealized syndrome measurements (right column). Average error-detected gate infidelity, or $\varepsilon_{\mathrm{pass}}$ (blue circles), is the state transfer fidelity of the evolution of the 36 cardinal two-qubit logical states (which can be shown to be equivalent to the average fidelity over the joint two-qubit space [67]) after postselection on $|g\rangle$, assuming no measurement error. We additionally calculate this infidelity in the presence of 1% (blue squares) and 5%(blue triangle) ancilla readout errors (see Appendix J). Gate failure results from a single jump error (a first-order error) happening during the gate, and therefore this probability scales linearly with coherence time. Since we can detect these errors, the error-detected gate infidelity is limited only by double-jump errors (second-order errors) and hence scales quadratically, allowing us to reach extremely low error-detected gate infidelities with typical coherence times. Numerical fits to illustrate these scalings are shown by the dashed blue and red lines (see Appendix L).

implies that an increase in coherence time by a factor of 10 yields a gate infidelity that decreases by a factor of 100.

Error-detected gates are immediately useful for near-term short-depth circuits and hence noisy intermediate-scale quantum era applications [22], where one can postselect for error-free circuit runs. Furthermore, error-detected gates at the hardware level can form the bedrock of a fully-error-corrected computation. Knowing exactly which gates had errors allows one to erase and reset the affected qubits. Stabilizer codes, including the surface code, are highly resilient to erasure errors [18–21]. The gate constructions we present are also transferable to other qubit platforms (see Appendix E), such as phonon modes in trapped ions, where one has access to conditional beam splitter interactions and where hyperfine states play the role of the ancilla [72]. We believe such hardware-level error detection offers a new direction in improving gates other than brute-force hardware improvement and broadens design considerations in developing novel quantum gates.

ACKNOWLEDGMENTS

We thank Shruti Puri, Patrick Winkel, Kevin C. Smith, Daniel K. Weiss, Sophia H. Xue, and Harshvardhan K. Babla for helpful discussions. We also appreciate critical feedback on the manuscript from Luigi Frunzio, Jahan Claes, and Alec Eickbusch. This research was supported by the U.S. Army Research Office under Grant No. W911NF-18-1-0212, and by the U.S. Department of Energy, Office of Science, National Quantum Information Science Research Centers, Co-design Center for Quantum Advantage, under Contract No. DE-SC0012704. The views and conclusions contained in this document are those of the authors and should not be interpreted as representing official policies, either expressed or implied, of

the U.S. Army Research Office or the U.S. Government. The U.S. Government. is authorized to reproduce and distribute reprints for Government purposes notwithstanding any copyright notation herein. We thank the Yale Center for Research Computing for technical support and high-performance computing resources. R.J.S. is a founder and shareholder of Quantum Circuits Inc.

APPENDIX A: DUAL-RAIL QUBITS

We discuss here how to apply the measurement and gate constructions to dual-rail qubits (Fig. 6). Dual-rail qubits differ from the other bosonic codewords we discuss because a logical qubit occupies two bosonic modes $(\hat{a}_1, \hat{b}_1)$ with codewords $|0\rangle_L = |01\rangle$ and $|1\rangle_L = |10\rangle_L$ Nonetheless, we can perform single-qubit logical Z gates by physically interacting with one of the bosonic modes in the dual-rail qubit. Explicitly, we can perform a Z gate via $Z_L = e^{i\pi \hat{a}_1^\dagger \hat{a}_1}$ or equivalently via $Z_L = e^{i\pi \hat{b}_1^\dagger \hat{b}_1}$. This means that even though two dual-rail qubits comprise four physical modes, only two of them need to interact to perform two-qubit logical gates and measurements. If we define $(\hat{a}_2, \hat{b}_2)$ as the modes in a second dual-rail qubit, we can perform a logical $ZZ_L(\theta)$ gate by using an ancilla coupled to mode $\hat{a}_2$ and setting $\widehat{P} = e^{i\pi(\hat{a}_1^\dagger \hat{a}_1 + \hat{a}_2^\dagger \hat{a}_2)}$.

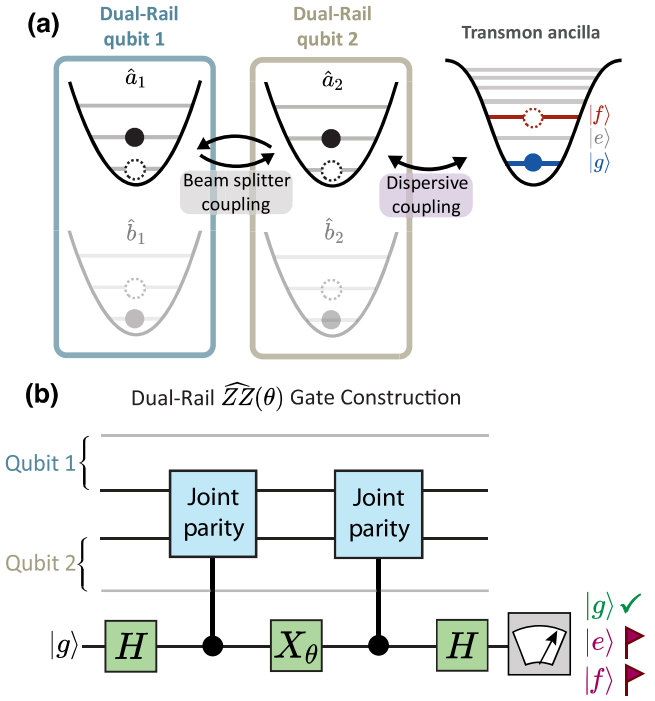

FIG. 6. Error-detected gates for dual-rail bosonic qubits. (a) Required hardware layout. Modes $(\hat{a}_1, \hat{b}_1)$ comprise qubit 1 and modes $(\hat{a}_2, \hat{b}_2)$ comprise qubit 2. An ancilla operated in the g-f manifold is dispersively coupled to $\hat{a}_2$, and we need a beam splitter interaction only between modes $\hat{a}_1$ and $\hat{a}_2$. (b) Gate construction for a $ZZ_L(\theta)$ gate for dual-rail qubits. We need to engineer the ancilla-controlled joint parity unitary acting on modes $\hat{a}_1$ and $\hat{a}_2$, where the joint parity operator is $e^{i\pi\left(\hat{a}_1^\dagger \hat{a}_1 + \hat{a}_2^\dagger \hat{a}_2\right)}$.

Another distinction with the dual-rail code is the fact that all logical gates conserve the total number of excitations in the system. Arbitrary single-qubit rotations in dual-rail qubits can be realized with the beam splitter interaction between the modes $\hat{a}_i$ and $\hat{b}_i$. When combined with the $ZZ_L(\theta)$ gate, this forms a universal gate set. In contrast, any bosonic code that uses only one bosonic mode per logical qubit by necessity requires gates that do not conserve the total number of excitations. For example an X gate in the Fock 0-1 code is $\hat{X}_{\text{Fock}} = |0\rangle\langle 1| + |1\rangle\langle 0|$, which involves transitions between states with different photon numbers, whereas $\hat{X}_{\text{dual rail}} = |01\rangle\langle 10| + |10\rangle\langle 01|$ does not.

For our gate and measurement constructions to be applied to the Fock 0-1 or dual-rail code, the modes must still be bosonic, with the ability to support up to two excitations in each mode. This is because constructions rely on Hong-Ou-Mandel-like interference when we start in the state $|11\rangle_{a_1,a_2}$. The dual-rail code also has the ability to detect photon loss errors after the gate or measurement. One or both of the dual-rail qubits may end in the state $|00\rangle_{a_i,b_i}$

APPENDIX B: DEFINITIONS OF THE BINOMIAL AND FOUR-LEGGED CAT CODES

The lowest-order binomial and four-legged cat codes are examples of bosonic encodings with twofold rotational symmetry. In other words, $Z_L = e^{i\pi/2 \hat{a}^\dagger \hat{a}}$, enabling us to perform $ZZ_L(\theta)$ gates with our proposed gate construction.

The logical codewords are defined for the lowest-order binomial code as follows:

$$|0_L\rangle = \frac{|0\rangle + |4\rangle}{\sqrt{2}}, \tag{B1}$$

$$|1_L\rangle = |2\rangle\,. \tag{B2}$$

The (even-photon-number) four-legged cat code is based on superpositions of coherent states and is defined as

$$|0_L\rangle = \frac{|\alpha\rangle + |i\alpha\rangle + |-\alpha\rangle + |-i\alpha\rangle}{\sqrt{N_0}}, \tag{B3}$$

$$|1_L\rangle = \frac{|\alpha\rangle - |i\alpha\rangle + |-\alpha\rangle - |-i\alpha\rangle}{\sqrt{N_1}}, \tag{B4}$$

where N_0 and N_1 are normalization factors. Both encodings share a similar photon number structure, with the $|0\rangle_L$ and $|1\rangle_L$ states containing the same average number of photons in the large-α limit. Codewords contain only an even number of photons, allowing photon loss to be detected via photon number parity measurements after our proposed gates.

APPENDIX C: INTERPRETATION OF GEOMETRIC PHASES ENCLOSED ON THE OPERATOR BLOCH SPHERE

A powerful resource we use is the geometric phase enclosed by trajectories on the operator Bloch sphere. For a qubit Bloch sphere, this phase is often just an irrelevant global phase, but in the operator Bloch sphere, this phase corresponds to performing a unitary of the form $\hat{R}_\phi = e^{i\phi/2(\hat{a}^\dagger\hat{a}+\hat{b}^\dagger\hat{b})}$, which acts on both bosonic modes. The mathematical reason behind this is because the effective angular momentum operator is given by $\hat{L}_I = \frac{1}{2}(\hat{a}^\dagger\hat{a} + \hat{b}^\dagger\hat{b})$, whereas for a qubit Bloch sphere, it takes the form $\hat{L}_I = \frac{1}{2}(|0\rangle\langle 0| + |1\rangle\langle 1|) = \frac{1}{2}\hat{\sigma}_0 = \mathbb{1}$. Enclosing phase ϕ on a "Bloch sphere" corresponds to performing the unitary $\hat{R}_\phi = e^{i\phi\hat{L}_I}$. This is a trivial global phase for the qubit Bloch sphere but a nontrivial unitary, $\hat{R}_\phi$ on the bosonic modes.

The value of ϕ is given geometrically by the solid angle enclosed by the trajectory, and physically corresponds to each mode $\hat{a}$ and $\hat{b}$ rotating by angle $\phi/2$ as described by the $\hat{R}_\phi$ unitary.

APPENDIX D: DERIVING USEFUL ANCILLA-CONTROLLED UNITARIES FROM THE DISPERSIVE BEAM SPLITTER HAMILTONIAN

The dispersive beam splitter Hamiltonian [Eq. (3)] allows a wide variety of ancilla-controlled unitaries to be constructed for different settings of the Hamiltonian parameters g, Δ, and φ. Even when these settings are fixed for the duration of the gate, we can realize several useful operations as listed in Table II and derived below.

1. Controlled SWAP operation

For the ancilla-controlled SWAP unitary, we wish to realize

$$\text{cSWAP} \equiv |g\rangle\langle g|\,\mathbb{1} + |f\rangle\langle f|\,\text{SWAP}. \tag{D1}$$

If the ancilla is in $|f\rangle$, we exchange the states in modes $\hat{a}$ and $\hat{b}$. If the ancilla is in $|g\rangle$, the states should be unaffected at the end of the operation. In the Heisenberg picture, one can write the desired mode transformations as

$$\begin{pmatrix}\hat{a}_g\\ \hat{b}_g\end{pmatrix} \to \begin{pmatrix}\hat{a}_g\\ \hat{b}_g\end{pmatrix}, \quad \begin{pmatrix}\hat{a}_f\\ \hat{b}_f\end{pmatrix} \to \begin{pmatrix}\hat{b}_f\\ \hat{a}_f\end{pmatrix}. \tag{D2}$$

Setting $\Delta = +|\chi|/2$ ensures that $\vec{n}_{|f\rangle}$ lies on the equator and that after time $T = \pi/g$ the mode transformations ($\hat{a}_f \to -i\hat{b}_f, \hat{b}_f \to -i\hat{a}_f$) will have been performed, which is a SWAP operation up to 90° cavity rotations.

We are still free to choose the parameter g. The goal is to find g such that the state precesses around vector $\vec{n}_g = (g, 0, \chi)/\sqrt{g^2+\chi^2}$ and such that $\hat{a}(t)$ returns to the pole after time $T = 2\pi/\sqrt{g^2+\chi^2}$.

Setting these times to be equal and solving for g,

$$\frac{2\pi}{\sqrt{g^2+\chi^2}} = \frac{\pi}{g}, \tag{D3}$$

gives $g = \chi/\sqrt{3}$ and duration $\sqrt{3}\pi/\chi$. The resulting mode transformations are

$$\begin{pmatrix}\hat{a}_g\\ \hat{b}_g\end{pmatrix} \to \begin{pmatrix}e^{i\pi\left(1-\sqrt{3}/2\right)}\hat{a}_g\\ e^{i\pi\left(1-\sqrt{3}/2\right)}\hat{b}_g\end{pmatrix}, \quad \begin{pmatrix}\hat{a}_f\\ \hat{b}_f\end{pmatrix} \to \begin{pmatrix}-i\hat{b}_f\\ -i\hat{a}_f\end{pmatrix}, \tag{D4}$$

which is almost the desired cSWAP operation. To fix the unwanted phase accumulations, one can add delay times before and after the unitary. The dispersive interaction acting for time t between mode $\hat{a}$ and the ancilla gives the mode transformations

$$\begin{pmatrix}\hat{a}_g\\ \hat{b}_g\end{pmatrix} \to \begin{pmatrix}\hat{a}_g\\ \hat{b}_g\end{pmatrix}, \quad \begin{pmatrix}\hat{a}_f\\ \hat{b}_f\end{pmatrix} \to \begin{pmatrix}e^{-i\chi t}\hat{a}_f\\ \hat{b}_f\end{pmatrix}. \tag{D5}$$

Adding a second delay after the ancilla-controlled unitary effectively implements a dispersive interaction between $\hat{b}_f$

TABLE II. Hamiltonian parameters for useful ancilla-controlled unitaries. The beam splitter rate g, detuning Δ, and gate duration are easily set by microwave drives in cQED hardware to match the conditions listed for useful operating points. The ancilla-state-dependent precession vectors $\vec{n}_{|g\rangle}$ and $\vec{n}_{|f\rangle}$ for the operator Bloch sphere are also listed. Controlled joint 4-parity unitaries allow one to implement logical $ZZ_L(\theta)$ gates for bosonic codewords with twofold rotational symmetry, such as the binomial and four-legged cat codes.

Operation	g	Δ	Duration	$\vec{n}_{\|g\rangle}$	$\vec{n}_{\|f\rangle}$
50:50 beam splitter	Any	$-\chi/2$	$\pi/2g$	$(1,0,0)$	...
Controlled SWAP	$1/\sqrt{3}\|\chi\|$	$+\chi/2$	$\sqrt{3}\pi/\|\chi\|$	$\left(\frac{1}{2},0,\sqrt{3}/2\right)$	$(1,0,0)$
Controlled joint parity	$\sqrt{3}/2\|\chi\|$	0	$2\pi/\|\chi\|$	$\left(\sqrt{3}/2,0,\frac{1}{2}\right)$	$\left(\sqrt{3}/2,0,-\frac{1}{2}\right)$
Controlled joint 4-parity (slow)	$\sqrt{7}/6\|\chi\|$	0	$3\pi/\|\chi\|$	$\left(\sqrt{7}/4,0,3/4\right)$	$\left(\sqrt{7}/4,0,-3/4\right)$
Controlled joint 4-parity (fast)	$\sqrt{15}/2\|\chi\|$	0	$\pi/\|\chi\|$	$\left(\sqrt{15}/4,0,1/4\right)$	$\left(\sqrt{15}/4,0,-1/4\right)$

and the ancilla since the modes have swapped. When one chooses $T = \pi/2|\chi|(3-\sqrt{3})$, the overall mode transformations are

$$\begin{pmatrix}\hat{a}_g\\ \hat{b}_g\end{pmatrix} \to \begin{pmatrix}e^{i\phi/2}\hat{a}_g\\ e^{i\phi/2}\hat{b}_g\end{pmatrix}, \quad \begin{pmatrix}\hat{a}_f\\ \hat{b}_f\end{pmatrix} \to \begin{pmatrix}e^{i\phi/2}\hat{b}_f\\ e^{i\phi/2}\hat{a}_f\end{pmatrix}, \tag{D6}$$

where $\phi = 2\pi\left(1-\sqrt{3}/2\right)$. These are the desired mode transformations for the cSWAP unitary up to the deterministic rotation $\hat{R}_\phi = e^{i\phi/2\left(\hat{a}^\dagger\hat{a}+\hat{b}^\dagger\hat{b}\right)}$ (which can be easily tracked in software). This trick can also be used to adjust geometric phase accumulation on a single mode.

2. Controlled joint parity operation

The joint parity operator $e^{i\pi\left(\hat{a}^\dagger\hat{a}+\hat{b}^\dagger\hat{b}\right)}$ is the ZZ_L operator for many bosonic codes, such as the Fock 0-1, dual-rail, and two-legged cat codes. The controlled joint parity unitary can be written as

$$\text{cJP} = |g\rangle\langle g|\,\mathbb{1} + |f\rangle\langle f|\,e^{i\pi\left(\hat{a}^\dagger\hat{a}+\hat{b}^\dagger\hat{b}\right)} \tag{D7}$$

up to the rotation operator $e^{-i\pi/2\left(\hat{a}^\dagger\hat{a}+\hat{b}^\dagger\hat{b}\right)}$, We can write the "symmetrized" controlled joint parity unitary

$$\begin{aligned}\text{cJP}_2 &= |g\rangle\langle g|\,e^{i\pi/2\left(\hat{a}^\dagger\hat{a}+\hat{b}^\dagger\hat{b}\right)} + |f\rangle\langle f|\,e^{-i\pi/2\left(\hat{a}^\dagger\hat{a}+\hat{b}^\dagger\hat{b}\right)}\\ &= |g\rangle\langle g|\,e^{i\pi\hat{L}_I} + |f\rangle\langle f|\,e^{-i\pi\hat{L}_I},\end{aligned} \tag{D8}$$

with the desired mode transformations

$$\begin{pmatrix}\hat{a}_g\\ \hat{b}_g\end{pmatrix} \to \begin{pmatrix}i\hat{a}_g\\ i\hat{b}_g\end{pmatrix}, \quad \begin{pmatrix}\hat{a}_f\\ \hat{b}_f\end{pmatrix} \to \begin{pmatrix}-i\hat{a}_f\\ -i\hat{b}_f\end{pmatrix}. \tag{D9}$$

We can obtain these mode transformations with precession vectors $\vec{n}_g$ and $\vec{n}_f$ that are antipodal to one another by setting $\Delta = 0$. This also means that the corresponding trajectories have equal precession rates given by $\Omega = \sqrt{g^2 + (\chi/2)^2}$ and return to the poles at the same time. The final step is to set the magnitude of g such that a solid angle ϕ is enclosed. For a precession vector with polar angle θ, the general formula for the solid angle is $\phi = 2\pi(1-\cos\theta)$. Therefore, for these precession vectors $|\phi| = 2\pi(1-\chi/2\Omega) = \pi$, which is solved by $g = \sqrt{3}/2\chi$ in time $T = 2\pi/\chi$. The trajectory for this operating point is that shown in Fig. 3(a).

3. Controlled joint 4-parity operation

The joint 4-parity operator, $e^{i\pi/2\left(\hat{a}^\dagger\hat{a}+\hat{b}^\dagger\hat{b}\right)}$, is the ZZ_L operator for bosonic codes with twofold rotational symmetry such as the binomial and four-legged cat codes. There exist different choices for symmetrized controlled joint 4-parity unitaries, each with their own operating point:

$$\text{cJP}_4^{\text{slow}} = |g\rangle\langle g|\,e^{i\pi/4\left(\hat{a}^\dagger\hat{a}+\hat{b}^\dagger\hat{b}\right)} + |f\rangle\langle f|\,e^{-i\pi/4\left(\hat{a}^\dagger\hat{a}+\hat{b}^\dagger\hat{b}\right)} \tag{D10}$$

or

$$\text{cJP}_4^{\text{fast}} = |g\rangle\langle g|\,e^{i3\pi/4\left(\hat{a}^\dagger\hat{a}+\hat{b}^\dagger\hat{b}\right)} + |f\rangle\langle f|\,e^{-i3\pi/4\left(\hat{a}^\dagger\hat{a}+\hat{b}^\dagger\hat{b}\right)}. \tag{D11}$$

One choice results in a faster unitary than the other. Both perform the controlled joint 4-parity unitary up to a rotation $\hat{R}_\phi$. In the slow case, a solid angle of $\pi/2$ must be enclosed, which is achieved for $g = \sqrt{7}/6\chi$ in time $3\pi/\chi$. In the fast case, a solid angle of $3\pi/2$ must be enclosed, which is achieved with $g = \sqrt{15}/2$ in time π/χ. The operator Bloch sphere trajectories are shown in Figs. 7(a) and 7(b).

4. Ancilla-controlled unitaries at smaller g/χ ratio

The ancilla-controlled unitaries we have considered thus far all rely on the ability to tune the magnitude of the beam splitter rate g to a specific value. In experiment, there may be restrictions that prevent one from reaching the required g/χ ratio. For each ancilla-controlled unitary, one can find alternative sets of Hamiltonian parameters that use a smaller g/χ ratio to implement an equivalent ancilla-controlled unitary but with a longer total duration. For example, to perform the cZZ operation one could instead perform two $\text{cJP}_4^{\text{slow}}$ unitaries back-to-back, which requires total gate duration $6\pi/\chi$ but approximately halves the required g/χ ratio.

The same logic can be applied to the cSWAP unitary. The trajectory for $\hat{a}(t)_{|g\rangle}$ may complete many orbits in the time it takes the $\hat{a}(t)_{|f\rangle}$ trajectory to reach the south pole of the operator Bloch sphere. The geometric phase accumulated depends on the number of orbits completed. When Δ is fixed to $\chi/2$, this condition may be written as

$$T = \frac{\pi}{g} = \frac{2\pi n}{\sqrt{g^2+\chi^2}} \tag{D12}$$

for $n = 1, 2, 3\ldots$.

5. Unconditional SWAP operation

A uSWAP operation refers to implementing the mode transformations

$$\begin{pmatrix}\hat{a}_g\\ \hat{b}_g\end{pmatrix} \to \begin{pmatrix}\hat{b}_g\\ \hat{a}_g\end{pmatrix}, \quad \begin{pmatrix}\hat{a}_f\\ \hat{b}_f\end{pmatrix} \to \begin{pmatrix}\hat{b}_f\\ \hat{a}_f\end{pmatrix}, \tag{D13}$$

in which the bosonic modes are swapped without regard to the state in the ancilla. In the operator Bloch sphere it

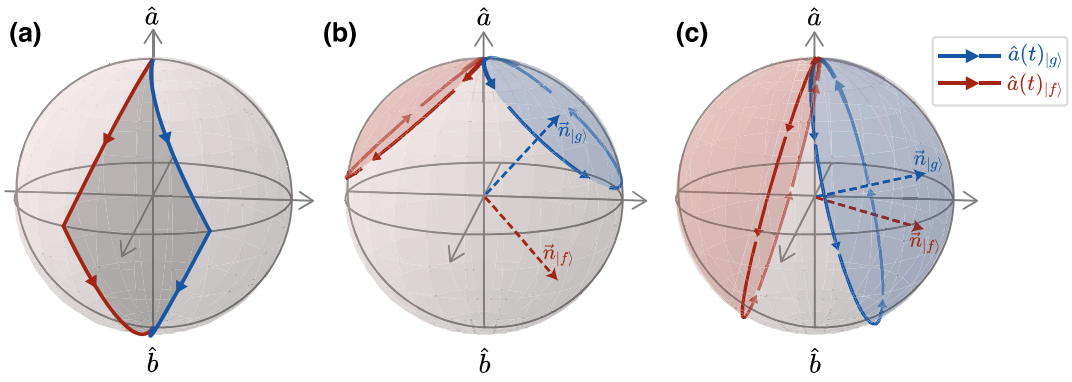

FIG. 7. Operator Bloch spheres showing the trajectories for $\hat{a}(t)$ and precession vectors during (a) unconditional SWAP, (b) controlled joint 4-parity (slow), and (c) controlled joint 4-parity (fast) operations. The trajectory in (a) is constructed piecewise from two different ancilla-controlled unitaries, where we apply a π pulse on the ancilla at the halfway point to reverse the $|g\rangle$ and $|f\rangle$ states.

is straightforward to realize the related mode transformations:

$$\begin{pmatrix}\hat{a}_g\\ \hat{b}_g\end{pmatrix}\to\begin{pmatrix}e^{i\phi/2}\hat{b}_g\\ e^{i\phi/2}\hat{a}_g\end{pmatrix},\quad \begin{pmatrix}\hat{a}_f\\ \hat{b}_f\end{pmatrix}\to\begin{pmatrix}e^{-i\phi/2}\hat{b}_f\\ e^{-i\phi/2}\hat{a}_f\end{pmatrix}. \tag{D14}$$

With appropriate delays before and after the unitary, one can again realize a "true" unconditional SWAP operation.

One way to realize the unitary described by Eq. (D14) is to set $g > \chi$ and $\Delta = 0$. After some time $T_{\rm eq}$, the trajectories $\hat{a}(t)_{|g\rangle}$ and $\hat{a}(t)_{|f\rangle}$ should reach the equator of the operator Bloch sphere simultaneously. At this time, one disables the beams splitter interaction and applies a π pulse on the ancilla to flip the $|f\rangle$ and $|g\rangle$ states. If the beam splitter interaction is re-enabled for time $T_{\rm eq}$, both trajectories will now travel toward the south pole and meet there. The complete trajectories are illustrated in Fig. 7(a), with the shaded area in between the trajectories equal to 2ϕ.

Performing an unconditional SWAP operation between bosonic modes can enable an ancilla coupled to one mode to interact with more than two different bosonic modes. As an example, if uSWAP_{1i} and $\text{c}Z_1$ operations are available, one can measure $\hat{Z}_1\hat{Z}_2\hat{Z}_3\hat{Z}_4$ stabilizers directly on four bosonic modes by first preparing the ancilla in $|+\rangle_{gf}$, implementing the unitary sequence $\text{c}Z_1-\text{uSWAP}_{12}-\text{c}Z_1-\text{uSWAP}_{13}-\text{c}Z_1-\text{uSWAP}_{14}-\text{c}Z_1$, and finally measuring the ancilla in the $|\pm\rangle_{gf}$ basis.

APPENDIX E: REALIZATION IN OTHER EXPERIMENTAL PLATFORMS

The operator Bloch sphere is applicable to other hardware platforms with access to a beam splitter interaction and an ancilla-controlled operation on a two-bosonic-mode system. In the main text, we considered Hamiltonian terms can be easily engineered in cQED,

$$\{\hat{a}^\dagger\hat{b}+\hat{a}\hat{b}^\dagger,\hat{a}^\dagger\hat{a},\hat{\sigma}^z\hat{a}^\dagger\hat{a}\}, \tag{E1}$$

where the dispersive interaction with an ancilla imparts a state-dependent frequency shift on one of the bosonic modes. This effectively produces an ancilla-dependent detuning between two bosonic modes, which we leverage in all proposed ancilla-controlled unitaries.

Alternatively, one can consider a gate set that includes a conditional beam splitter interaction:

$$\{\hat{\sigma}^z(\hat{a}^\dagger\hat{b}+\hat{a}\hat{b}^\dagger),\hat{a}^\dagger\hat{b}+\hat{a}\hat{b}^\dagger,\hat{a}^\dagger\hat{a}\}. \tag{E2}$$

This gate set is realized in trapped-ion systems where phononic modes serve as bosons and hyperfine states play the role of the ancilla [73–75]. By setting the amplitude, phase, and detuning of the unconditional beam splitter drive, one can engineer ancilla-state-dependent precession vectors and trajectories on the operator Bloch sphere.

APPENDIX F: CONSTRUCTING AN ARBITRARY, EXCITATION-PRESERVING TWO-QUBIT GATE

With parameterized $\text{eSWAP}(\theta)$ and $ZZ_L(\theta)$ gates, one can construct any two-qubit gate that conserves the total number of excitations in the encoded subspace. A general excitation-preserving two-qubit gate can be parameterized by the following circuit:

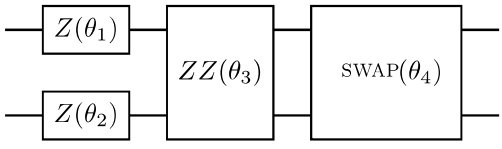

With particular choices of $\theta_1,\theta_2,\theta_3$, and θ_4, one can generate useful gate families:

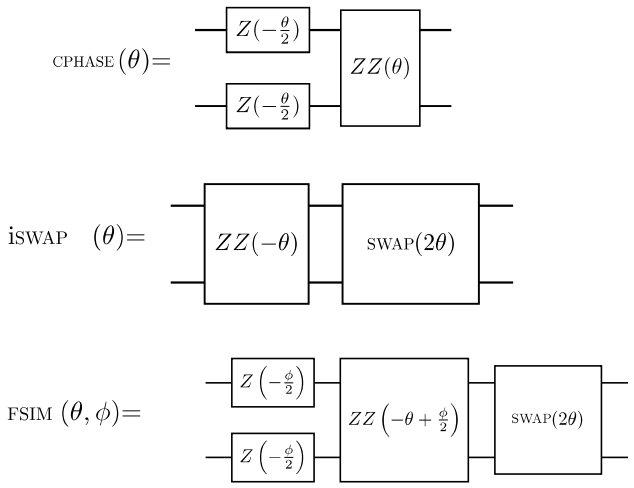

CZ $=$ CPHASE$(\pi/2)$ is locally equivalent to a controlled NOT gate, which is often used as the basic two-qubit gate in general quantum circuits. On the other hand, parameterized iSWAP(θ) and fSIM(θ_1,θ_2) are useful for efficiently compiling near-term algorithms, which leverages the excitation-conserving nature of the gate to simulate particular quantum chemistry problems whose electronic structure involves number-conserving symmetry [76].

APPENDIX G: HAMILTONIAN ENGINEERING FOR ERROR-CORRECTED OR ERROR-DETECTED GATES

1. The error closure condition

What are the formal requirements for hardware errors that occur during a gate to be detectable or correctable at the end of the gate? Previous work on error-correctable gates relied on error transparency[77], but in this work we recognize that error transparency is a stronger condition than necessary for a gate to be error-correctable. Here we describe a new, less stringent condition that still guarantees that a gate is error-correctable (or error-detectable), which we call "error closure". For brevity, we set $\hbar = 1$ here.

We consider gate unitary U implemented by the time evolution of the Hamiltonian $\widehat{\mathcal{H}}_0$ such that $U = e^{-i\widehat{\mathcal{H}}_0 T}$. First, we reiterate the requirements for $\widehat{\mathcal{H}}_0$ to be transparent to a set of hardware errors $\{\hat{\epsilon}\}_{\text{hardware}}$ that may occur at any time during the gate:

$$[\widehat{\mathcal{H}}_0, \hat{\epsilon}] = 0, \tag{G1}$$

$$\forall \hat{\epsilon} \in \{\hat{\epsilon}\}_{\text{hardware}}. \tag{G2}$$

If one is able to correct for errors from $\{\hat{\epsilon}\}_{\text{hardware}}$ affecting idle qubits, error transparency ensures that one can also correct these errors if they occur during the gate by performing error correction after the gate.

This condition generalizes to detectable errors as well as correctable errors. $\{\hat{\epsilon}\}_{\text{hardware}}$ is error-detectable if one can perform syndrome measurements that indicate whether an error in the set occurred, but one cannot know (or cannot implement) the correction unitary on the states. This can occur when different errors yield the same error syndrome, or when the unknown time of a jump error means that one cannot know what the appropriate correction unitary should be. In the main text, we defined a gate to be error-detectable if one can detect any one jump error from $\{\hat{\epsilon}\}_{\text{hardware}}$ occurring during the gate via syndrome measurements after the gate.

There exist counterexamples (such as the $\widehat{ZZ}_L$ measurement) that are error-correctable operations but that are not error-transparent. The error closure formalism is used to evaluate the effects of jump errors from $\{\hat{\epsilon}\}_{\text{hardware}}$. The effects of no-jump backaction are not included in the error closure formalism, and we consider them separately in our gate and measurement constructions later, although their effect is usually small and of second order.

We first define a larger set of errors $\{\hat{\epsilon}\}_{\text{corr}}$ that contains all the errors one can correct for. We assume that one has independent error correction operations (syndrome measurement and recovery) for each error in $\{\hat{\epsilon}\}_{\text{hardware}}$. It follows that if $\hat{\epsilon}_i, \hat{\epsilon}_j \in \{\hat{\epsilon}\}_{\text{hardware}}$, one can correct superpositions of errors such as $c_i\hat{\epsilon}_i + c_j\hat{\epsilon}_j$ and products of errors such as $\hat{\epsilon}_i\hat{\epsilon}_j$ for $i \neq j$. The fact that $\{\hat{\epsilon}\}_{\text{corr}}$ encompasses a larger set of errors than $\{\hat{\epsilon}\}_{\text{hardware}}$ is what allows us to relax the error transparency condition and search for a less strict condition for error correction.

We now define our error closure conditions for the Hamiltonian $\widehat{\mathcal{H}}_0$ and the error set $\{\hat{\epsilon}\}_{\text{hardware}}$. First we generate a new set of errors $\{\hat{\epsilon}\}_{\text{ext}}$ from every possible commutator between $\widehat{\mathcal{H}}_0$ and the elements of $\{\hat{\epsilon}\}_{\text{hardware}}$,

$$[\widehat{\mathcal{H}}_0, \hat{\epsilon}_{\text{hardware}}] = \hat{\epsilon}_{\text{ext}}, \tag{G3}$$

as well as linear combinations of these commutators. Error closure is satisfied if

(1) $\hat{\epsilon}_{\text{ext}} \in \{\hat{\epsilon}\}_{\text{corr}}$.
(2) $[\widehat{\mathcal{H}}_0, \hat{\epsilon}_{\text{ext}}] \in \{\hat{\epsilon}\}_{\text{ext}}$.

These conditions state that the errors generated by Eq. (G3) must form a closed set of correctable errors and ensure that hardware errors during the gate remain correctable errors after the gate. We now sketch the proof.

Jump evolution for a hardware error $\hat{\epsilon}$ occurring at time $T - t$ during the gate evolution can be written as

$$e^{-i\widehat{\mathcal{H}}_0 t}\hat{\epsilon}e^{-i\widehat{\mathcal{H}}_0(T-t)} = e^{-i\widehat{\mathcal{H}}_0 t}\hat{\epsilon}e^{i\widehat{\mathcal{H}}_0 t}e^{-i\widehat{\mathcal{H}}_0 T}. \tag{G4}$$

The condition for hardware errors to be correctable is

$$e^{-i\widehat{\mathcal{H}}_0 t}\hat{\epsilon}e^{i\widehat{\mathcal{H}}_0 t} \in \{\hat{\epsilon}\}_{\text{corr}}, \tag{G5}$$

$$\forall \hat{\epsilon} \in \{\hat{\epsilon}\}_{\text{hardware}}, \tag{G6}$$

$$\forall t \in [0, T]. \tag{G7}$$

Our error closure conditions ensure this is satisfied. From the Baker-Campbell-Hausdorff theorem, we may write

$$e^{-i\widehat{\mathcal{H}}_0 t}\hat{\epsilon}e^{i\widehat{\mathcal{H}}_0 t} \tag{G8}$$

$$= \hat{\epsilon} + i[\widehat{\mathcal{H}}_0, \hat{\epsilon}]t - [\widehat{\mathcal{H}}_0, [\widehat{\mathcal{H}}_0, \hat{\epsilon}]]\frac{t^2}{2!} - i[\widehat{\mathcal{H}}_0, [\widehat{\mathcal{H}}_0, [\widehat{\mathcal{H}}_0, \hat{\epsilon}]]]\frac{t^3}{3!} + \cdots . \tag{G9}$$

The error closure conditions ensure the nested commutation relations produce errors that are only in $\{\hat{\epsilon}\}_{\text{corr}}$, and hence the entire Taylor series is also in $\{\hat{\epsilon}\}_{\text{corr}}$ since it is a superposition of correctable errors. If $\widehat{\mathcal{H}}_0^{(1)}$ and $\widehat{\mathcal{H}}_0^{(2)}$ both satisfy error closure, then so does $\widehat{\mathcal{H}}_0^{(1)} + \widehat{\mathcal{H}}_0^{(2)}$. Note that satisfying the error transparency condition automatically satisfies the error closure conditions. It also follows that if a correctable error occurs before the gate, it will still be correctable after the gate. We now give explicit examples to show how this framework can be used.

2. Example A: Photon loss in beam splitter interactions

Suppose one wishes to perform a SWAP operation between two bosonic modes by actuating the Hamiltonian $\widehat{\mathcal{H}}_0 = g/2(\hat{a}^\dagger\hat{b} + \hat{a}\hat{b}^\dagger)$ for time $T = \pi/g$. We choose a bosonic encoding that allows us to correct single-photon loss after the SWAP operation via photon number parity measurements, such as the binomial code or the four-legged cat code. The hardware errors we consider are $\{\hat{\epsilon}\}_{\text{hardware}} = \{\hat{a}, \hat{b}\}$, and the errors one can correct on idle qubits are $\{\hat{\epsilon}\}_{\text{corr}} = \{\hat{a}, \hat{b}, \hat{a}\hat{b}, c_0\hat{a} + c_1\hat{b} + c_2\hat{a}\hat{b}\}$. We show how one can correct for photon loss errors at intermediate times, even when outside the logical codespace. From Eq. (G3) one finds

$$[\hat{a}^\dagger\hat{b} + \hat{a}\hat{b}^\dagger, \hat{a}] = -\hat{b}, \tag{G10}$$

$$[\hat{a}^\dagger\hat{b} + \hat{a}\hat{b}^\dagger, \hat{a}] = -\hat{a}, \tag{G11}$$

but when evaluating the commutator with error $\hat{a}\hat{b}$, one finds

$$\left[\hat{a}^\dagger\hat{b} + \hat{a}\hat{b}^\dagger, \hat{a}\hat{b}\right] = -\hat{b}^2 - \hat{a}^2, \tag{G12}$$

which generates errors outside the set of correctable errors, and so $\hat{a}\hat{b}$ is not in $\{\hat{\epsilon}\}_{\text{ext}}$. After evaluating all the commutators, one finds $\{\hat{\epsilon}\}_{\text{ext}} = \{c_0\hat{a} + c_1\hat{b}\} \subset \{\hat{\epsilon}\}_{\text{corr}}$.

Thus, $\widehat{\mathcal{H}}_0$ and $\{\hat{\epsilon}\}_{\text{hardware}}$ satisfy the error closure conditions for the SWAP operations. This means that one can correct for $\hat{a}$ and $\hat{b}$ errors during the gate without requiring error transparency and despite evolving the states outside the codespace.

3. Example B: Ancilla-controlled unitaries generated by $\widehat{\mathcal{H}}_{\chi\text{BS}}$

The gate and measurement constructions have favorable error detection and error correction properties because the Hamiltonians used to generate the ancilla-controlled unitaries satisfy error closure—here we show why. We consider hardware errors $\{\hat{\epsilon}\}_{\text{hardware}} = \{\hat{a}, \hat{b}, \hat{\sigma}_z^{gf}\}$ where transmon ancilla decay is treated separately by use of the $|e\rangle$ level of the ancilla for error detection.

We set $\widehat{\mathcal{H}}_0 = g/2(\hat{a}^\dagger\hat{b} + \hat{a}\hat{b}^\dagger) + (\Delta + \chi/2\hat{\sigma}_z^{gf})\hat{a}^\dagger\hat{a}$. With an appropriate bosonic code, one can detect photon loss via parity measurements and ancilla dephasing via the flag state $|f\rangle$ (in the gate construction) or repeated measurements (for the measurement construction in Fig. 8):

$$\{\hat{\epsilon}\}_{\text{corr}} = \{\hat{a}, \hat{b}, \hat{\sigma}_z^{gf}, \hat{a}\hat{\sigma}_z^{gf}, \hat{b}\hat{\sigma}_z^{gf}, \hat{a}\hat{b}, \hat{a}\hat{b}\hat{\sigma}_z^{gf}\}, \tag{G13}$$

where we now omit the linear combinations from $\{\hat{\epsilon}\}_{\text{corr}}$ for clarity. By writing out the commutation relations

$$\left[\widehat{\mathcal{H}}_0, \hat{a}\right] = -\frac{g}{2}\hat{b} - \left(\Delta + \frac{\chi}{2}\hat{\sigma}_z^{gf}\right)\hat{a}, \tag{G14}$$

$$\left[\widehat{\mathcal{H}}_0, \hat{b}\right] = -\frac{g}{2}\hat{a}, \tag{G15}$$

$$\left[\widehat{\mathcal{H}}_0, \hat{\sigma}_z^{gf}\right] = 0, \tag{G16}$$

we begin to find the elements in $\{\hat{\epsilon}\}_{\text{ext}}$. We calculate the next order of commutators, $[\widehat{\mathcal{H}}_0, [\widehat{\mathcal{H}}_0, \hat{\epsilon}]]$, to arrive at the closed error set

$$\{\hat{\epsilon}\}_{\text{ext}} = \{\hat{a}, \hat{b}, \hat{\sigma}_z^{gf}, \hat{a}\hat{\sigma}_z^{gf}, \hat{b}\hat{\sigma}_z^{gf}\} \subset \{\hat{\epsilon}\}_{\text{corr}}, \tag{G17}$$

and so the error closure conditions are satisfied for each of the ancilla-controlled unitaries $\hat{U}_c$.

Hardware errors midway through $\hat{U}_c$ can lead to complicated errors. For example, photon loss at an unknown time results in the operator $(c_0\hat{a} + c_1\hat{b})e^{i\varphi\hat{\sigma}_z^{gf}}\hat{U}_c$ being applied to the system, where the coefficients c_0, c_1, snd φ all depend on the exact time of the photon loss. Despite one not knowing this time or these coefficients, the error can still be corrected.

No-jump backaction associated with photon loss does not form part of the error closure formalism but can be evaluated by considering whether the photon number populations depend on the ancilla states $|g\rangle$ and $|f\rangle$. For cZZ$_L$

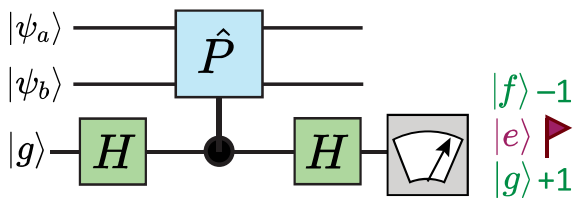

FIG. 8. Circuit for performing QND measurements of binary-valued operator $\widehat{P}$ from ancilla-controlled unitaries. If χ matching is satisfied, we can error-correct the dominant errors in the ancilla and bosonic modes.

unitaries, the photon number distributions of the bosonic modes are independent of the ancilla states. Visually, this means that trajectories on the operator Bloch sphere have the same latitude at all points in time, and hence no-jump backaction due to photon loss or ancilla decay is absent. This is not true for cSWAP operations, although it is generally a small effect.

4. Suitable Hamiltonians for error closure

One can engineer many different Hamiltonian terms on bosonic modes via processes such as four-wave mixing with a transmon in cQED. When exploring exclusively bosonic codes designed to correct discrete photon loss errors, we find that only the lowest-order interactions are suitable, as detailed in Table III.

APPENDIX H: ERROR-CORRECTED MEASUREMENTS

Here we examine the measurements that can be constructed from ancilla-controlled unitaries and the errors that can be corrected. The circuit used to perform this measurement is shown in Fig. 8. If $\hat{P}$ is a binary-valued operator with eigenvalues ± 1, this circuit performs a QND measurement of $\hat{P}$.

TABLE III. Error closure for candidate Hamiltonians for bosonic codes designed to protect from single-photon loss. For bosonic codes designed to correct against single-photon loss, we can evaluate the commutator $[\widehat{\mathcal{H}}_0, \hat{a}]$ to see if the Hamiltonian could satisfy error closure. We find only the lowest-order Hamiltonians make good candidates for constructing gates. In the table, if $\widehat{\mathcal{H}}_0$ is a good candidate, so is $\widehat{\mathcal{H}}_0 \otimes \hat{\sigma}_z^{gf}$.

$\widehat{\mathcal{H}}_0$	$[\widehat{\mathcal{H}}_0, a]$	$\widehat{\mathcal{H}}_0$ and $\{a, b\}$ satisfy error closure?
$a^\dagger a$	a	✓
$a + a^\dagger$	1	✓
$ab^\dagger + a^\dagger b$	b	✓
$a^\dagger b^\dagger + ab$	$b^\dagger$	✗
$a^{\dagger 2} + a^2$	$2a^\dagger$	✗
$a^\dagger a(b + b^\dagger)$	$a(b + b^\dagger)$	✗
$(a + a^\dagger)b^\dagger b$	$b^\dagger b$	✗
$a^\dagger a b^\dagger b$	$ab^\dagger b$	✗

The simpler structure of this circuit means that one can both detect *and* correct errors from $\{\hat{a}, \hat{b}, \hat{\sigma}_z^{gf}, |e\rangle\langle f| + \text{h.c.}\}$ that occur during the circuit. This measurement can be considered as the two-mode extension of the fault-tolerant parity measurement presented in Ref. [34].

To correct ancilla decay $|e\rangle\langle f| + \text{h.c.}$, one must now also engineer "χ matching" ($\chi = \chi_{ge} = \chi_{gf}$) as in Refs. [33,34]. If $|e\rangle$ is measured at the end of the circuit, then decay likely happened during $\hat{U}_c$. By contextuality, this means the ancilla started in $|f\rangle$ at the beginning of $\hat{U}_c$. χ matching ensures that one knows with certainty which unitary has been applied to the bosonic modes even though the precise time of the decay is unknown. This unitary is the one generated by $\widehat{\mathcal{H}}_f = g_{\text{bs}}/2(\hat{a}^\dagger\hat{b} + \hat{a}\hat{b}^\dagger) + (\Delta + \chi/2)\,\hat{a}^\dagger\hat{a} = \widehat{\mathcal{H}}_e$ acting for the duration of $\hat{U}_c$. For measurements where $\widehat{P} = \text{SWAP}$ or ZZ_L, this will be identity, SWAP, or a unitary of the form $e^{i\phi\left(\hat{a}^\dagger\hat{a} + \hat{b}^\dagger\hat{b}\right)}$, all of which are straightforward to correct for in cQED. Afterwards one can retry the measurement. We now describe how to correct the remaining errors in $\{\hat{\epsilon}\}_{\text{hardware}} = \{\hat{a}, \hat{b}, \hat{\sigma}_z^{gf}\}$

We first consider errors from this set occurring during $\hat{U}_c$, the longest duration unitary in the measurement circuit. As a sequence of successive unitaries applied from right to left, the gate sequence reads

$$e^{-i\pi/4\hat{Y}_{gf}}\,\hat{U}_c e^{i\pi/4\hat{Y}_{gf}}. \tag{H1}$$

Hardware errors during $\hat{U}_c$ result in a sequence of unitaries equivalent to

$$e^{-i\pi/4\hat{Y}_{gf}}\,\hat{\epsilon}\,\hat{U}_c e^{i\pi/4\hat{Y}_{gf}} = \hat{\epsilon}' e^{-i\pi/4\hat{Y}_{gf}}\,\hat{U}_c e^{i\pi/4\hat{Y}_{gf}}, \tag{H2}$$

where $\hat{\epsilon}'$ can be a superposition of errors from the set $\{\hat{a}, \hat{b}, \hat{a}\hat{\sigma}_x^{gf}, \hat{b}\hat{\sigma}_x^{gf}\}$, which is also a set that satisfies the error closure condition for $\hat{\mathcal{H}}_{\chi\text{BS}}$. (Note that commuting through $\pi/2$ pulses changes $\hat{\sigma}_z^{gf}$ for $\hat{\sigma}_x^{gf}$, meaning the measurement outcomes $|g\rangle$ and $|f\rangle$ can be flipped.) In words, this means ancilla dephasing during $\hat{U}_c$ does not affect the bosonic modes but results in a high chance (50%) of observing $|f\rangle$ instead of $|g\rangle$, and vice versa.

Photon loss errors during $\hat{U}_c$ are equivalent to ancilla dephasing during the measurement accompanied by photon loss occurring after the measurement, which can be detected or tracked [66] via fault-tolerant parity measurements [34] and then corrected.

For completeness, we also consider ancilla dephasing during the short ancilla rotations, which is equivalent to measuring or initializing the ancilla in the wrong basis. Again, the $|g\rangle$ and $|f\rangle$ measurement outcomes may be flipped, but a backaction of the form $c_0\mathbb{1} + c_1\widehat{P}$ may also be imparted on the bosonic modes for unknown c_0 and c_1.

Once again, this error can be corrected by repeating the measurement until correctly projecting the states into an eigenstate of $\widehat{P}$. Importantly, this backaction conserves the $\widehat{P}$ eigenvalue that makes this error-correctable. In general, g or f measurement errors in the measurement construction are correctable by repeating the measurement and taking a majority vote on the outcomes.

As an example, we describe how one might perform an error-corrected ZZ_L measurement on two qubits encoded in the binomial code. First, one repeats ZZ_L measurements until one observes enough $|g\rangle$ or $|f\rangle$ outcomes to perform a majority vote and obtain a ZZ_L eigenvalue. Then one must check that no photon loss occurred during the measurements, which would invalidate the majority vote. This can be done by performing parity measurements on individual modes.

If both modes are of even parity, the measured ZZ_L eigenvalue will be reliable—the ZZ_L measurements yield useful information only if both bosonic modes are in even-photon-number states. If any modes have an odd number of photons, one must apply the error correction unitary for photon loss in the binomial code and repeat the entire measurement until the photon loss checks are satisfied. Although the sequence involves many measurements to majority vote on both the ZZ_L measurements and the parity measurements, the complete procedure fully corrects errors in $\{\epsilon\}_{\text{hardware}}$.

APPENDIX I: ERRORS IN THE ERROR-DETECTED GATE CONSTRUCTION

Despite using the same $\hat{U}_c$ building blocks as the measurements, the gate construction can fundamentally only detect errors in $\{\epsilon\}_{\text{hardware}}$ not correct them. This is because of the way ancilla dephasing errors commute through the entire gate construction. Depending on whether they happen in the first or the second $\hat{U}_c$, they have the same flag state $|f\rangle$ but impart different unitaries on the bosonic modes. Since we are designing a gate that detects only ancilla errors, we do not need to engineer χ matching. Whenever the ancilla is observed to be in $|e\rangle$ at the end of the gate, a decay error (which may have occurred at any point during the gate construction) is indicated. No-jump backaction associated with the $|e\rangle\langle f|$ decay can be mitigated by over-rotating the ancilla by slightly more than $\pi/2$ in the first ancilla rotation.

Upon detecting $|e\rangle$, we must reset the state in the bosonic mode, which in general will have leaked out of the codespace. This is because we will be at some unknown point on the operator Bloch sphere (and only evolution that brings us back to the poles can leave us back in the codespace). To see why, we can consider ancilla decay that occurs during the first cZZ_L unitary. The quantum trajectory can be described by our applying the Hamiltonian $\mathcal{H} = g/2\left(a^\dagger b + ab^\dagger\right) + \chi_{gf}\, a^\dagger a$ for some time t_{jump} and then the Hamiltonian $\mathcal{H} = g/2\left(a^\dagger b + ab^\dagger\right) + \chi_{ge} a^\dagger a$ for the remaining time $T_{\text{gate}} - t_{\text{jump}}$. Since t_{jump} is unknown, we end up at an unknown point on the operator Bloch sphere.

An important consequence of this is that a fraction of $\varepsilon_{\text{pass}}$ will be leakage errors, due to undetected double-decay events in the ancilla. Depending on the choice of bosonic encodings, this slow buildup of leakage errors may be easy to detect and reset with additional operations. For instance, in the dual-rail encoding, QND joint parity measurements suffice to detect leakage.

The gate construction ideally performs the unitary

$$\widehat{U}_{\text{gate}}(\theta) \otimes |g\rangle\langle g| + \widehat{U}_{\text{gate}}(-\theta) \otimes |f\rangle\langle f|, \tag{I1}$$

where $\widehat{U}_{\text{gate}}(\theta)$ is the desired entangling gate on the bosonic modes. This unitary can be performed by sequentially applying the following sequences of unitaries to the system, provided the ancilla is initialized in its ground state

$$e^{-i\pi/4\hat{Y}_{gf}}\, \widehat{U}_c e^{-i\theta/2\hat{X}_{gf}}\, \widehat{U}_c e^{i\pi/4\hat{Y}_{gf}}, \tag{I2}$$

We now investigate the effects of ancilla dephasing. Photon loss errors also dephase the ancilla, so analyzing this error resolves the issue of error propagation resulting from the hardware errors $\{\hat{a}, \hat{b}, \hat{\sigma}_z^{gf}\}$. Ancilla dephasing $\hat{\sigma}_z^{gf}$ that happens during the first $\widehat{U}_c$ results in the overall gate unitary

$$e^{-i\pi/4\hat{Y}_{gf}}\, \widehat{U}_c e^{-i\theta/2\hat{X}_{gf}}\, \widehat{U}_c \hat{\sigma}_z^{gf}\, e^{i\pi/4\hat{Y}_{gf}} \tag{I3}$$

$$= e^{-i\pi/4\hat{Y}_{gf}}\, \widehat{U}_c e^{-i\theta/2\hat{X}_{gf}}\, \widehat{U}_c e^{i\pi/4\hat{Y}_{gf}}\, \hat{\sigma}_x^{gf} \tag{I4}$$

$$= \widehat{U}_{\text{gate}}(\theta)\hat{\sigma}_x^{gf} \tag{I5}$$

$$= \hat{\sigma}_x^{gf}\, \widehat{U}_{\text{gate}}(-\theta). \tag{I6}$$

In other words, the ancilla ends in $|f\rangle$, and the incorrect unitary $\widehat{U}_{\text{gate}}(-\theta)$ is applied to the bosonic modes.

Dephasing that occurs during the second $\hat{U}_c$ results in the overall gate unitary $\hat{\sigma}_z \widehat{U}_{\text{gate}}(\theta)$. The ancilla ends in $|f\rangle$, and the correct gate unitary $\widehat{U}_{\text{gate}}(\theta)$ is applied. From these two scenarios, if the ancilla is observed to be in $|f\rangle$, it is unknown whether the unitary $\widehat{U}_{\text{gate}}(-\theta)$ or the unitary $\widehat{U}_{\text{gate}}(\theta)$ was applied, and only this error is detectable.

We also show that one can still detect ancilla dephasing even if it occurs during any of the three short ancilla rotations. This means that the error-detected gate fidelity should not be limited by ancilla decoherence during the rotations (i.e. transmon gate fidelities in cQED). If ancilla dephasing happens during the final $e^{-i\pi/4\hat{Y}_{gf}}$ rotation, the ancilla and the bosonic modes are disentangled by this stage. One still performs $\widehat{U}_{\text{gate}}(\theta)$ correctly but there is now a probability that the ancilla is detected in $|f\rangle$. Dephasing during the first $e^{i\pi/4\hat{Y}_{gf}}$ rotation is equivalent to starting

the ancilla in a random $c_0 |g\rangle + c_1 |f\rangle$ superposition. Thus, when one measures the ancilla in $|g\rangle$, the correct gate unitary will have also been performed. Dephasing during the middle pulse $e^{-i\theta/2\hat{X}_{gf}}$ rotation results in applying the gate $\widehat{U}_{\text{gate}}(\theta_{\text{random}})$, where θ_{random} depends on the exact time of the dephasing jump during the middle pulse. This error is also flagged because the ancilla will also end in the $|f\rangle$ state.

The gate construction is not robust with regard to second-order ancilla dephasing. On roughly half of the occasions where two $\hat{\sigma}_z$ jumps occur during the gate, they will occur during different ancilla-controlled unitaries. The net result is that the incorrect unitary $\hat{U}(-\theta)$ is applied to the bosonic modes *and* the ancilla is measured in state $|g\rangle$ at the end of the gate, so this error is not flagged. Logically, this error corresponds to a Pauli ZZ error affecting both bosonic qubits.

Photon loss errors also cause dephasing on the ancilla [34] and thus can be detected only at the end of the gate construction (e.g. via parity measurements).

APPENDIX J: SIMULATION DETAILS

A $ZZ_L(\theta)$ gate is simulated by numerically solving the Lindblad master equation under the static dispersive Hamiltonian and the controls needed to realize the constituent operations (specifically, beam splitters and transmon pulses):

$$\widehat{\mathcal{H}}_{\chi\text{BS}} = \widehat{\mathcal{H}}_{\chi} + \widehat{\mathcal{H}}_{\text{BS}}(t) + \widehat{\mathcal{H}}_{T}(t). \tag{J1}$$

The static Hamiltonian describes the dispersive coupling to the ancilla with a frequency shift for each ancilla basis state:

$$\begin{aligned}\widehat{\mathcal{H}}_{\chi}/\hbar = -\hat{a}^\dagger\hat{a}\Big(&\frac{\chi_f}{2}|g\rangle\langle g| \\ &+\Big(\frac{\chi_f}{2}-\chi_e\Big)|e\rangle\langle e| \\ &-\frac{\chi_f}{2}|f\rangle\langle f|\Big),\end{aligned} \tag{J2}$$

where we choose $\chi_e/2\pi = -0.5$ MHz and $\chi_f/2\pi = -1$ MHz. We have written this Hamiltonian in a frame where the dispersive interaction for $|g\rangle$ and $|f\rangle$ is symmetric. We assume the time-dependent beam splitter and transmon drives to be piecewise-constant throughout the protocol and constant when realizing each unitary in the gate construction. This allows us to ignore the effects of any particular choice of pulse shape, since we wish to highlight how the overall protocol fidelity scales with various error rates. Furthermore, because the beam splitter and transmon pulses are never simultaneous, we can define distinct time-independent Hamiltonians corresponding to beam splitter operations and transmon operations:

$$\begin{aligned}\widehat{\mathcal{H}}_{\text{BS}}/\hbar &= \frac{g}{2}\left(\hat{a}^\dagger\hat{b} + \hat{a}\hat{b}^\dagger\right) + \Delta\hat{a}^\dagger\hat{a}, \\ \widehat{\mathcal{H}}_{T}/\hbar &= \epsilon_x\hat{\sigma}_x^{gf} + \epsilon_y\hat{\sigma}_y^{gf},\end{aligned} \tag{J3}$$

where ϵ_x and ϵ_y are the drive strengths of the two control quadratures coupled to the g-f manifold Pauli operators $\hat{\sigma}_x^{gf} = |f\rangle\langle g| + |g\rangle\langle f|$ and $\hat{\sigma}_y^{gf} = i|f\rangle\langle g| - i|g\rangle\langle f|$. Because the $ZZ_L(\theta)$ gate uses the cZZ_L operation, we take $\Delta = 0$ throughout the gate sequence. During transmon operations, we ignore the dispersive coupling, as this can also be compensated for with appropriate pulse shaping.

We then use this Hamiltonian in the Lindblad master equation:

$$\frac{d\rho}{dt} = -i\left[\widehat{\mathcal{H}},\rho\right] + \Gamma_1^T\mathcal{D}[\hat{t}]\rho + \Gamma_\phi^T\mathcal{D}[\hat{t}^\dagger\hat{t}]\rho + \Gamma_1^C\mathcal{D}[\hat{a}]\rho, \tag{J4}$$

where $\hat{t} = |g\rangle\langle e| + \sqrt{2}|e\rangle\langle f|$ is the annihilation operator for the transmon mode, $\mathcal{D}[\hat{\mathcal{L}}]\rho = \hat{L}\rho\hat{L}^\dagger - \frac{1}{2}\hat{L}^\dagger\hat{L}\rho - \frac{1}{2}\rho\hat{L}^\dagger\hat{L}$ is the usual Lindblad dissipator, $\Gamma_1^T = 1/T_1^{|g\rangle\langle e|}$, $\Gamma_\phi^T = 1/T_\phi^{|e\rangle\langle e|}$, and $\Gamma_1^C = 1/T_1^{\text{loss}}$.

The Lindblad equation can also be expressed in terms of a Liouvillian $\widehat{\mathcal{L}}$ as

$$\frac{d\rho}{dt} = -i\widehat{\mathcal{L}}\rho, \tag{J5}$$

where $\widehat{\mathcal{L}}\rho = \left[\widehat{\mathcal{H}},\rho\right] + i\Gamma_1^T\mathcal{D}[\hat{t}]\rho + i\Gamma_\phi^T\mathcal{D}[\hat{t}^\dagger\hat{t}]\rho + i\Gamma_1^C\mathcal{D}[\hat{a}]\rho$. Because the transmon and beam splitter drives are either enabled or disabled for each of the five steps in a given protocol, we can express the final state density matrix after the whole sequence described in Fig. 4 as

$$\rho^f = \widehat{\mathcal{U}}_{T_3}\widehat{\mathcal{U}}_{B_2}\widehat{\mathcal{U}}_{T_2}\widehat{\mathcal{U}}_{B_1}\widehat{\mathcal{U}}_{T_1}\rho^i, \tag{J6}$$

where each $\widehat{\mathcal{U}}_j = e^{-i\widehat{\mathcal{L}}_j t}$ is the (generally *non-unitary*) propagator under the time-independent Liouvillian corresponding to a transmon pulse $\widehat{\mathcal{U}}_T$ or beam splitter pulse $\widehat{\mathcal{U}}_B$ in the presence of errors.

We then prepare the 36 cardinal states of the joint logical space ρ_k^i as

$$\begin{aligned}\{\rho^i : |\psi\rangle\otimes|\phi\rangle\ \forall\ |\psi\rangle,|\phi\rangle \in \\ \{|0_L\rangle,|1_L\rangle, \\ \frac{1}{\sqrt{2}}(|0_L\rangle + |1_L\rangle), \frac{1}{\sqrt{2}}(|0_L\rangle - |1_L\rangle), \\ \frac{1}{\sqrt{2}}(|0_L\rangle + i|1_L\rangle), \frac{1}{\sqrt{2}}(|0_L\rangle - i|1_L\rangle)\}\}\end{aligned} \tag{J7}$$

and simulate the evolution of each one under the sequence of Liouvillians for a given protocol, yielding a final density

operator ρ_k^f. We choose these states because the average trace fidelity over these states yields the trace fidelity over the entire joint logical subspace [67].

Next we simulate measurement of the ancilla. In a small fraction of measurements, one will erroneously measure an ancilla in the $|e\rangle$ state or the $|f\rangle$ state as being in $|g\rangle$. Therefore, to simulate an imperfect ancilla measurement, we first calculate the system density matrices that would result from perfect ancilla measurements for the ancilla in its three basis states. The traces of these density matrices are the probabilities of observing the ancilla in a particular state, and therefore we take the gate failure probability to be $1 - \mathrm{Tr}\left[|g\rangle\langle g|\,\rho_k^f\right]$.

We then compute a weighted sum of these density matrices to find the mixed logical state resulting from an imperfect observation of $|g\rangle$, with weights given by the probability of misassigning a particular state. The overall model is expressed as

$$\rho_k^p = \sum_{\psi\in g,e,f} \eta_{g\psi}\,|\psi\rangle\langle\psi|\rho_k^f|\psi\rangle\langle\psi|, \tag{J8}$$

where $\eta_{g\psi}$ is the probability of observing $|g\rangle$ when the state was $|\psi\rangle$. In cQED, most of the readout error comes from decay of the transmon during the readout pulse itself; therefore, we set $\eta_{gg} = 1 - 10^{-4}$ on the basis of the distinguishability of ancilla pointer states in a typical integrated readout signal [78]. Given typical readout pulse lengths, we compute the results for $\eta_{ge} = 0.01$ and 0.05. In all cases we assume that $\eta_{gf} = \eta_{ge}^2$ [17]. Tracing over the ancilla states yields the resulting mixed density matrix conditioned on an imperfect postselection measurement.

We then simulate the detection of errors in the bosonic modes by using the appropriate syndrome measurements for the dual-rail and binomial codes. For the dual-rail code with basis states $\{|01\rangle, |10\rangle\}$, the occurrence of decays can be detected by measuring joint photon-number parity on each pair of dual-rail modes and observing an odd outcome for both. We can therefore write

$$\begin{aligned}\hat{M} = &|0_L\rangle\langle 0_L| \otimes |0_L\rangle\langle 0_L| \\ &+ |0_L\rangle\langle 0_L| \otimes |1_L\rangle\langle 1_L| \\ &+ |1_L\rangle\langle 1_L| \otimes |0_L\rangle\langle 0_L| \\ &+ |1_L\rangle\langle 1_L| \otimes |1_L\rangle\langle 1_L|,\end{aligned} \tag{J9}$$

where $|0\rangle_L = |01\rangle$ and $|1\rangle_L = |10\rangle$. For the binomial code, photon-number parity measurements are used for syndrome measurements, and therefore the corresponding measurement operator is

$$\hat{M} = \left(\frac{\mathbb{1} + e^{i\pi(\hat{a}^\dagger\hat{a})}}{2}\right)\left(\frac{\mathbb{1} + e^{i\pi(\hat{b}^\dagger\hat{b})}}{2}\right). \tag{J10}$$

After simulating idealized syndrome checks, we can write the state of the modes conditioned on observing no error as

$$\rho_k^{p,M} = \hat{M}\rho_k^p\hat{M}^\dagger. \tag{J11}$$

Finally, we renormalize this density matrix to obtain $\tilde{\rho}_k^{p,M}$ and compute the overlap with the pure state obtained by applying the perfect gate unitary $\hat{U}$ to the initial state. We average the post-selected state transfer fidelities associated with the gate over the 36 cardinal states to obtain

$$\varepsilon_{\mathrm{pass}} = \frac{1}{36}\sum_k \mathrm{Tr}\left(\tilde{\rho}_k^{p,M}\hat{U}\rho_k^i\hat{U}^\dagger\right). \tag{J12}$$

APPENDIX K: IMPACT OF DEVICE NONIDEALITIES

In cQED, the dispersive Hamiltonian is only an approximation, with known higher-order corrections. The next-highest-order terms are the self-Kerr of each bosonic mode and cross-Kerr between bosonic modes, as well as higher-order corrections to the dispersive interaction itself. Although these are typically a factor of 100–1000 times weaker than χ, they present a source of coherent error unaccounted for in the proposed gate design. Here we quantify their effects on gate performance for realistic experimental parameters.

The higher-order corrections are modeled with the Hamiltonian

$$\hat{\mathcal{H}}_{NL}/\hbar = -\frac{K_a}{2}\hat{a}^\dagger\hat{a}^\dagger\hat{a}\hat{a} - \frac{K_b}{2}\hat{b}^\dagger\hat{b}^\dagger\hat{b}\hat{b} \tag{K1}$$

$$+ \hat{a}^\dagger\hat{a}^\dagger\hat{a}\hat{a}\left(\chi_f'\,|f\rangle\langle f| + \chi_e'\,|e\rangle\langle e|\right) \tag{K2}$$

$$+ \chi_{ab}\hat{a}^\dagger\hat{a}\hat{b}^\dagger\hat{b}, \tag{K3}$$

where K_a and K_b are the self-Kerrs of each bosonic mode, χ_e'a and χ_f' are higher-order corrections to the dispersive interaction, and χ_{ab} is the cross-Kerr between the bosonic modes, which may result from both modes participating in the nonlinear element used to actuate the beam splitter coupling.

What is the expected error induced by these terms? We can write the rates associated with these corrections as $\tilde{K} \sim (K_a, K_b, \chi_f', \chi_{ab})$. As a rough approximation, these terms add a state-dependent detuning to the bosonic modes of order approximately $\bar{n}\tilde{K}$, where $\bar{n}$ is the average photon number in the modes. From our intuition for single-qubit gates on a Bloch sphere, this detuning will cause the state to miss its target by a small distance proportional to approximately $\bar{n}\tilde{K}$, which includes the possibility of moving off the surface of the sphere due to distortion of the logical state. Since fidelity is quadratic in the state overlap, our ancilla-controlled unitaries should be only quadratically sensitive to this detuning, with an infidelity expected to scale as $\sim (\bar{n}\tilde{K}\tau_{\mathrm{gate}})^2 \sim \left(\bar{n}\tilde{K}/\chi_f\right)^2$.

When designing a device for experiment, we can control χ_f through the geometry of the device. Increasing the value of this parameter causes τ_{gate} to decrease linearly but $\tilde{K}$ to increase *quadratically*. Therefore, reducing χ_f will always reduce the gate error from $\hat{\mathcal{H}}_{NL}$. On the other hand, reducing χ_f will always increase the errors due to decoherence by increasing τ_{gate}. These competing effects mean there is an optimal value of χ_f to engineer.

Additional simulations displayed in Fig. 9 highlight the competition between nonlinearity and decoherence. From typical values we measure in experiment [33], we assume an initial operating point where $\chi_f'/2\pi = 2$ kHz, $\chi_e'/2\pi = 1.125$ kHz, and $K_a/2\pi = K_b/2\pi = 2$ kHz when $\chi_f/2\pi = -1$ MHz, and that these quantities would scale quadratically if we were to vary χ_f. We also assume $\chi_{ab}/2\pi = 100$ Hz for all χ_f, chosen to reflect values attainable in modern hardware [41]. For the transmon pulse, we again ignore the dispersive interaction and its higher-order corrections.

The rightmost column in Fig. 9 shows that in the absence of decoherence, the error associated with nonlinearity scales quadratically in χ_f as expected. The leftmost and center columns in Fig. 9 highlight that when decoherence is introduced, the benefits of a weaker coupling to the nonlinear ancilla are overridden by the increased incoherent error experienced by the slower gate. This leads to an optimum that may be found for different bosonic codes and decoherence rates. For the codes and parameters explored here, we find the optimal χ_f to be approximately 1 MHz and observe persistent error-detected gate infidelities on the order of 0.01% or below.

APPENDIX L: ERROR SCALING PREFACTORS FOR DIFFERENT ERROR CHANNELS AND BOSONIC CODES

The simulation results shown in Fig. 5 show that gate failure scales linearly and error-detected gate infidelity scales quadratically with each hardware decoherence rate considered. The fits take the form $A_n\left(\tau_{\text{gate}}/T_{\text{coh}}\right)^n$. For a given error channel, we find A_2 is significantly smaller than A_1 (and often much smaller than 1), granting further protection against second-order hardware errors; here we explain this observation.

We begin with the case of photon loss. The probability of single-photon loss occurring determines A_1. For the binomial code, there are an average of two photons in each bosonic mode, for a total of four photons. Hence, $A_1 \approx 4$ for the gate failure probability. Similarly, for the dual-rail code, $A_1 \approx 2$. Double-photon loss in the binomial code sets A_2 for the error-detected gate infidelity. The probability of double-photon loss is $\frac{1}{2}\left(\frac{\bar{n}\tau_{\text{gate}}}{T_{\text{coh}}}\right)^2$, where the factor of $1/2$ comes from the fact that photon loss must occur sequentially in a given time window. Half of the time, double-photon loss results in the detectable error $\hat{a}\hat{b}$. Overall, this means that $A_2 = \bar{n}^2/4 \approx 1$

For the gate failure probability resulting from ancilla errors, $A_1 \approx 1$. A single ancilla error results in a failed gate. The values of A_2 for ancilla errors require more detailed analysis. For ancilla dephasing, if two σ_z errors occur within the same ancilla-controlled unitary, they cancel each other out. Only if they occur in different ancilla-controlled unitaries do they cause a gate error, and hence we pick up a factor of $1/2$. When this error happens, the applied gate is $ZZ_L(-\pi/2)$, which causes an error on half of the cardinal states, yielding another factor of $1/2$. Overall, this makes $A_2 \approx 1/4$ for ancilla dephasing.

Finally, A_2 for ancilla decay is the most involved to calculate. Double-decay errors require decay to $|e\rangle$, then to $|g\rangle$. The $|g\rangle\langle e|$ decay rate is presumed to be half the $|e\rangle\langle f|$ decay rate, yielding an initial factor of $1/2$. Decay to $|e\rangle$ must happen before decay to $|g\rangle$ in the same time window, giving the next factor of $1/2$. Most of the time, double decay to $|g\rangle$ will leave the system in a random ancilla state in the g-f manifold due to the ancilla rotations in the sequence, and hence double decays are detected as $|f\rangle$ at the end of the sequence half of the time. Finally, we assume that when double decay happens, the bosonic modes may be outside the codespace but still have some overlap with the target states. This quantity is difficult to calculate. We define it as $A_{\text{leak}} < 1$. Overall, this means that $A_1 = A_{\text{leak}}/8 < 1/8$ for double ancilla decay errors. In general, these combinatoric factors help further suppress the effects of second-order ancilla errors.

APPENDIX M: PULSE SHAPING FOR $ZZ_L(\theta)$ GATES

Here we show by an example how pulse shaping can be used for future experimental realizations of the $ZZ_L(\theta)$ gate, which addresses the practical constraint of finite pulse bandwidth. We find pulse shaping can fix two unwanted effects that arise from finite pulse bandwidth: unwanted dynamics during the gradual ramping up of our beam splitter amplitude, g, and unwanted dynamics during the short-duration but finite-duration transmon rotations. These unwanted dynamics are due to the "always-on" nature of the dispersive interaction between the transmon and the cavity mode in the cQED systems we consider. Crucially, we show that simple pulse shaping solutions do not dramatically increase the duration or complexity of the gate. The full pulse sequence example is illustrated in Fig. 10.

To engineer our example pulse, we split the $ZZ_L(\theta)$ gate into five parts that are individually optimized: three ancilla rotations and two identical cZZ_L unitaries. For simplicity, we examine the $ZZ_L(\pi/2)$ gate in the Fock 0-1 encoding. We use optimal control pulses found with gradient ascent pulse engineering (GRAPE) and simple pulse detunings to

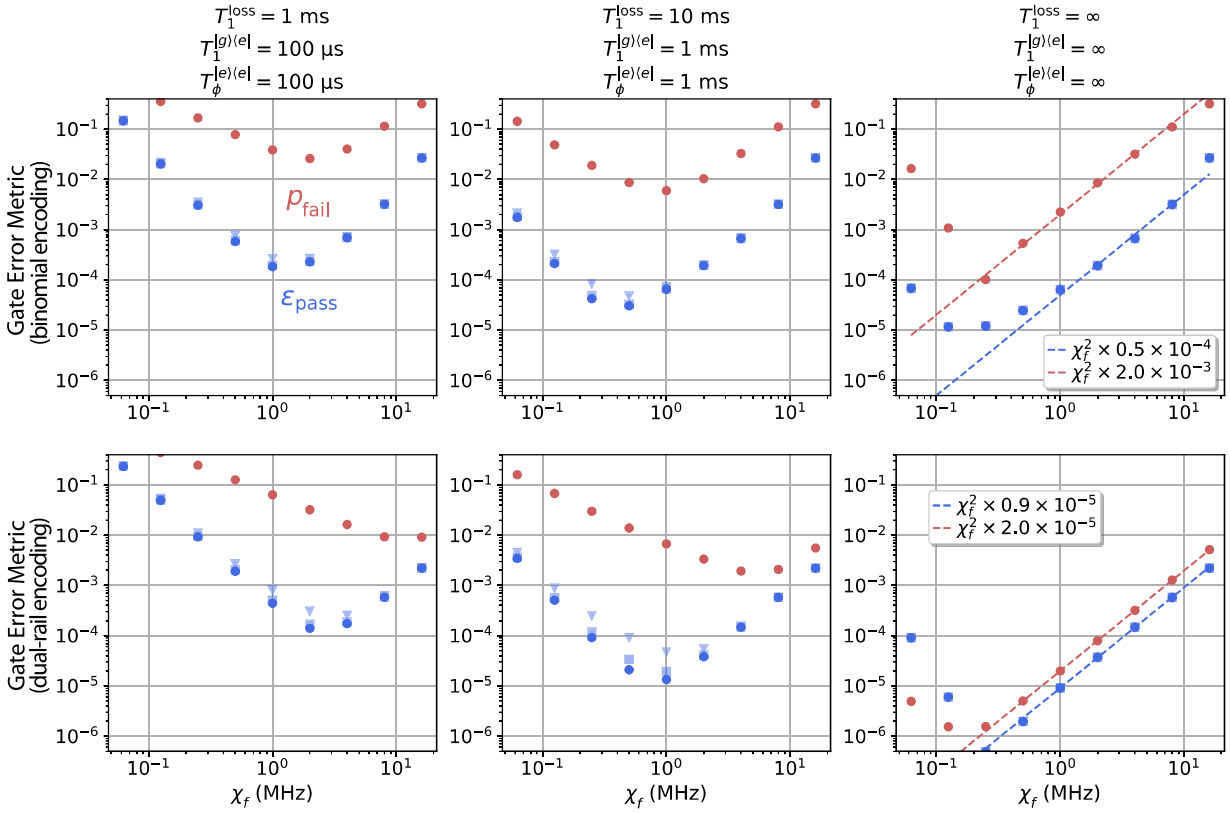

FIG. 9. Impact of undesired nonlinearities due to ancilla coupling. Average gate failure probability (red circles) and average error-detected gate infidelity (blue circles) for three sets of coherence parameters as functions of χ_f. The resulting infidelities and error probabilities scale quadratically with χ_f, as shown with fits to the simulation data (dashed blue and red lines). Reducing χ_f allows one to reduce the strengths of cavity self-Kerr and higher-order corrections to the dispersive interaction, but increases the impact of decoherence and cross-Kerr, leading to the emergence of an optimal operating point. Having 99% measurement error (blue squares) or 95% measurement error has a small but sometimes noticeable impact on the resulting logical infidelity.

compose our example pulse sequence. By analyzing the subsequent dynamics with QuTiP master equation simulations, we verify we can perform the gate with coherent errors of approximately 0.01% and with expected error-detected gate infidelities of approximately 0.01%, showing how we can overcome finite-bandwidth effects without compromising the key benefits of our gate.

Transmon rotations within the $|g\rangle$-$|f\rangle$ manifold are expected to take 50–100 ns with current hardware, since we must be careful to avoid unwanted leakage to the $|e\rangle$ level (although this error is also detectable). We use GRAPE to find pulse $\epsilon_d(t) = \epsilon_x(t) + i\epsilon_y(t)$ with the Hamiltonian

$$\mathcal{H} = \epsilon_d(t)\,|f\rangle\langle g| + \epsilon_d^*(t)\,|g\rangle\langle f| + \frac{\chi}{2}\left(|g\rangle\langle g| - |f\rangle\langle f|\right)\hat{a}^\dagger\hat{a},$$

working in the frame where $\Delta = \chi/2$ and the constraint that the transmon reaches the equator state $(|g\rangle + |f\rangle)/\sqrt{2} = |+\rangle_{gf}$ after 100 ns, regardless of whether there is one photon or there are zero photons in cavity mode $\hat{a}$ (see Fig. 2 for reference). Future work should also explicitly model the transmon's anharmonicity in the Hamiltonian to minimize leakage to $|e\rangle$ in the pulse. Here we assume our transmon drive can directly drive transitions between the $|g\rangle$ level and the $|f\rangle$ level.

We find our numerically optimized pulses closely resemble Gaussian $3\pi/2$ pulses (rather than $\pi/2$ pulses) to reach $|+\rangle_{gf}$. A similar pulse is also found for the final transmon rotation, which takes $|+\rangle_{gf}$ to $|g\rangle$. For the intermediate transmon rotation, we use a detuned Gaussian pulse of duration 40 ns, also with an amplitude close to what would be required for a $3\pi/2$ pulse. We chose the detuning and phase such that the transmon state stays as close as possible to the equator plane of the $|g\rangle$-$|f\rangle$ Bloch sphere.

To preserve error detection with regard to transmon dephasing errors, we should adhere to what we call the "equal latitude condition" as closely as possible throughout the gate. That is, the latitude of the transmon on its $|g\rangle$-$|f\rangle$ Bloch sphere should remain independent of the state in the cavities at all times during the gate. We can see in Fig. 10(c) that this is mostly the case for our

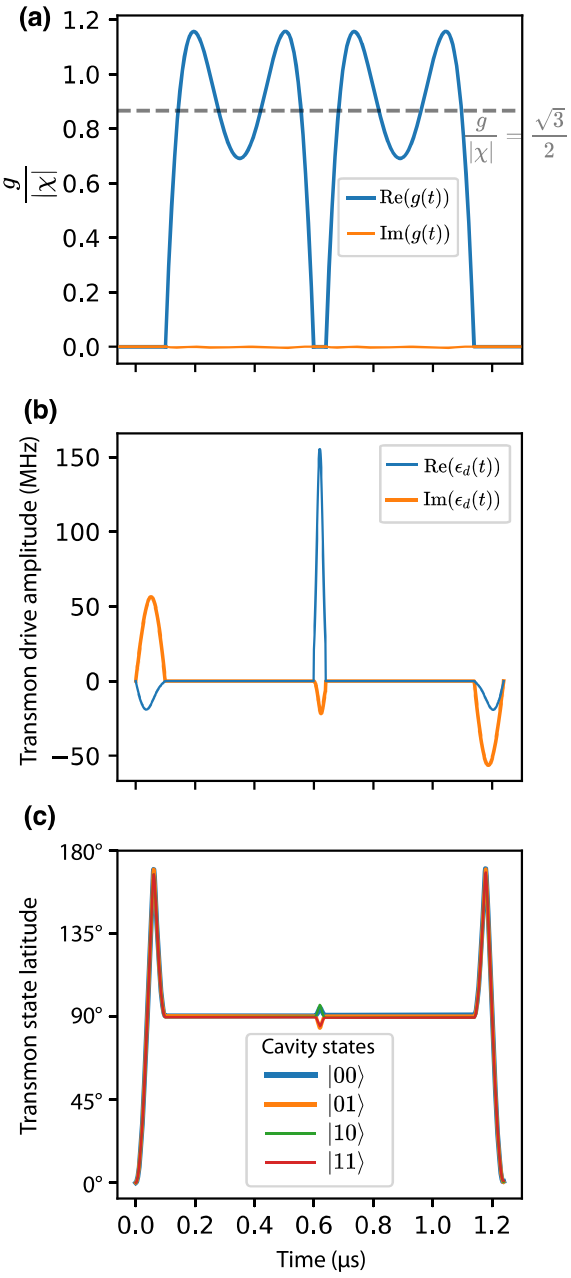

FIG. 10. Example of pulse shaping for a $ZZ(\pi/2)$ gate in the Fock 0-1 encoding. We work in the frame $\Delta = \chi/2$ for all drives. (a) GRAPE pulse for the beam splitter drive. The dashed line indicates the beam splitter strength required if we were to use rectangular (instantaneous ramp-up) pulses. (b) Pulse shaping for the three ancilla rotations during the $ZZ(\pi/2)$ gate. All pulses closely resemble Gaussian $3\pi/2$ pulses. The first and last pulses are found with GRAPE. The middle pulse is a simple detuned Gaussian $3\pi/2$ pulse that parameterizes the gate angle, θ. (c) Latitude of the transmon on its $|g\rangle$-$|f\rangle$ Bloch sphere, showing that the dynamics respect the "equal latitude condition" for the four different possible cavity states.

numerically optimized pulse, except for the intermediate transmon rotation, where there is a slight deviation. While we can no longer error-detect 100% of transmon dephasing events during this rotation, as far as we can tell, this does not noticeably limit our error-detected gate fidelity in this particular pulse. Future pulse optimization efforts should take this equal latitude condition into account in the cost function, which seems to be a more general requirement for being able to detect ancilla dephasing errors.

Pulses for the cZZ_L unitary are found from the Hamiltonian

$$\mathcal{H} = \frac{1}{2}\left(g(t)a^\dagger b + g^*(t)ab^\dagger\right) + \frac{\chi}{2}a^\dagger a\left(|g\rangle\langle g| - |f\rangle\langle f|\right),$$

with the constraint $g(0) = g(2\pi/\chi) = 0$. The solutions we find generally require $g_{\max}$ to be slightly larger than $\sqrt{3}/2\chi$.

The total gate duration for $\chi/2\pi = 2$ MHz is 1240 ns, which is close to the $4\pi/\chi = 1000$ ns limit for the fastest gate time possible with our construction. The actual unitary we implement is $ZZ(\pi/2)Z_1(\theta_1)$, where the additional single-qubit Z rotation is an artifact of the static dispersive interaction. For this particular pulse, $\theta_1 = 0.03$, an almost negligible effect. In the absence of decoherence, we obtain an average gate infidelity of 0.015% and an average failure probability of 0.039% (both due to coherent control errors).

We expect the average gate infidelity to be only quadratically sensitive to pulse shaping errors. When we model the pulse amplitude error by increasing all pulse amplitudes by 0.5%, we obtain an average gate infidelity of 0.030% and an average failure probability of 0.065%. Similarly, when we detune all pulses by +10 kHz, we obtain an average gate infidelity of 0.030% and an average failure probability of 1.8%, mainly from detuned ancilla pulses.

When we set $T_1^{|g\rangle\langle e|} = 100$ μs, $T_\phi^{|e\rangle\langle e|} = 100$ μs, and $T_1^{\mathrm{loss}} = \infty$, we find an average gate failure probability of 2.4% and an average error-detected gate infidelity of 0.019%, demonstrating that we maintain low error rates. (Including photon loss, we estimate an additional 0.2% failure probability if we were to use this pulse sequence for the dual-rail encoding with $T_1^{\mathrm{loss}} = 1$ ms per cavity.)

[1] J. Koch, T. M. Yu, J. Gambetta, A. A. Houck, D. I. Schuster, J. Majer, A. Blais, M. H. Devoret, S. M. Girvin, and R. J. Schoelkopf, Charge-insensitive qubit design derived from the Cooper pair box, Phys. Rev. A **76**, 042319 (2007).

[2] H. Paik, D. I. Schuster, L. S. Bishop, G. Kirchmair, G. Catelani, A. P. Sears, B. R. Johnson, M. J. Reagor, L. Frunzio, L. I. Glazman, S. M. Girvin, M. H. Devoret, and R. J. Schoelkopf, Observation of High Coherence in Josephson Junction Qubits Measured in a Three-Dimensional Circuit QED Architecture, Phys. Rev. Lett. **107**, 240501 (2011).

[3] A. P. M. Place, *et al.*, New material platform for superconducting transmon qubits with coherence times exceeding 0.3 milliseconds, Nat. Commun. **12**, 1779 (2021).

[4] C. Ballance, T. Harty, N. Linke, M. Sepiol, and D. Lucas, High-Fidelity Quantum Logic Gates Using Trapped-Ion Hyperfine Qubits, Phys. Rev. Lett. **117**, 060504 (2016).
[5] L. DiCarlo, J. M. Chow, J. M. Gambetta, L. S. Bishop, B. R. Johnson, D. I. Schuster, J. Majer, A. Blais, L. Frunzio, S. M. Girvin, and R. J. Schoelkopf, Demonstration of two-qubit algorithms with a superconducting quantum processor, Nature **460**, 240 (2009).
[6] Y. Chen, *et al.*, Qubit Architecture with High Coherence and Fast Tunable Coupling, Phys. Rev. Lett. **113**, 220502 (2014).
[7] K. X. Wei, E. Magesan, I. Lauer, S. Srinivasan, D. F. Bogorin, S. Carnevale, G. A. Keefe, Y. Kim, D. Klaus, W. Landers, N. Sundaresan, C. Wang, E. J. Zhang, M. Steffen, O. E. Dial, D. C. McKay, and A. Kandala, Quantum crosstalk cancellation for fast entangling gates and improved multi-qubit performance, (2021), ArXiv:2106.00675.
[8] P. H. Leung, K. A. Landsman, C. Figgatt, N. M. Linke, C. Monroe, and K. R. Brown, Robust 2-Qubit Gates in a Linear Ion Crystal Using a Frequency-Modulated Driving Force, Phys. Rev. Lett. **120**, 020501 (2018).
[9] E. Torrontegui, D. Heinrich, M. I. Hussain, R. Blatt, and J. J. García-Ripoll, Ultra-fast two-qubit ion gate using sequences of resonant pulses, New J. Phys. **22**, 103024 (2020).
[10] Y. Sung, L. Ding, J. Braumüller, A. Vepsäläinen, B. Kannan, M. Kjaergaard, A. Greene, G. O. Samach, C. McNally, D. Kim, A. Melville, B. M. Niedzielski, M. E. Schwartz, J. L. Yoder, T. P. Orlando, S. Gustavsson, and W. D. Oliver, Realization of High-Fidelity CZ and *ZZ*-Free iSWAP Gates with a Tunable Coupler, Phys. Rev. X **11**, 021058 (2021).
[11] C. Monroe, R. Raussendorf, A. Ruthven, K. R. Brown, P. Maunz, L.-M. Duan, and J. Kim, Large-scale modular quantum-computer architecture with atomic memory and photonic interconnects, Phys. Rev. A **89**, 022317 (2014).
[12] L. Egan, D. M. Debroy, C. Noel, A. Risinger, D. Zhu, D. Biswas, M. Newman, M. Li, K. R. Brown, M. Cetina, and C. Monroe, Fault-tolerant control of an error-corrected qubit, Nature **598**, 281 (2021).
[13] T. Olsacher, L. Postler, P. Schindler, T. Monz, P. Zoller, and L. M. Sieberer, Scalable and Parallel Tweezer Gates for Quantum Computing with Long Ion Strings, PRX Quantum **1**, 020316 (2020).
[14] L. Postler, S. Heußen, I. Pogorelov, M. Rispler, T. Feldker, M. Meth, C. D. Marciniak, R. Stricker, M. Ringbauer, R. Blatt, P. Schindler, M. Müller, and T. Monz, Demonstration of fault-tolerant universal quantum gate operations, Nature **605**, 675 (2022).
[15] F. Arute, *et al.*, Quantum supremacy using a programmable superconducting processor, Nature **574**, 505 (2019).
[16] P. Jurcevic, *et al.*, Demonstration of quantum volume 64 on a superconducting quantum computing system, Quantum Sci. Technol. **6**, 025020 (2021).
[17] S. S. Elder, C. S. Wang, P. Reinhold, C. T. Hann, K. S. Chou, B. J. Lester, S. Rosenblum, L. Frunzio, L. Jiang, and R. J. Schoelkopf, High-Fidelity Measurement of Qubits Encoded in Multilevel Superconducting Circuits, Phys. Rev. X **10**, 011001 (2020).
[18] T. M. Stace, S. D. Barrett, and A. C. Doherty, Thresholds for Topological Codes in the Presence of Loss, Phys. Rev. Lett. **102**, 200501 (2009).
[19] Y. Wu, S. Kolkowitz, S. Puri, and J. D. Thompson, Erasure conversion for fault-tolerant quantum computing in alkaline earth Rydberg atom arrays, Nat. Commun. **13**, 4657 (2022).
[20] A. Kubica, A. Haim, Y. Vaknin, F. Brandão, and A. Retzker, Erasure qubits: Overcoming the T_1 limit in superconducting circuits, (2022), ArXiv:quant-ph/2208.05461.
[21] M. Kang, W. C. Campbell, and K. R. Brown, Quantum error correction with metastable states of trapped ions using erasure conversion, (2022), ArXiv:2210.15024.
[22] J. Preskill, Quantum computing in the NISQ era and beyond, Quantum **2**, 79 (2018).
[23] A. Wallraff, D. I. Schuster, A. Blais, L. Frunzio, R.-S. Huang, J. Majer, S. Kumar, S. M. Girvin, and R. J. Schoelkopf, Strong coupling of a single photon to a superconducting qubit using circuit quantum electrodynamics, Nature **431**, 162 (2004).
[24] M. Reagor, W. Pfaff, C. Axline, R. W. Heeres, N. Ofek, K. Sliwa, E. Holland, C. Wang, J. Blumoff, K. Chou, M. J. Hatridge, L. Frunzio, M. H. Devoret, L. Jiang, and R. J. Schoelkopf, Quantum memory with millisecond coherence in circuit QED, Phys. Rev. B **94**, 014506 (2016).
[25] M. H. Michael, M. Silveri, R. Brierley, V. V. Albert, J. Salmilehto, L. Jiang, and S. Girvin, New Class of Quantum Error-Correcting Codes for a Bosonic Mode, Phys. Rev. X **6**, 031006 (2016).
[26] P. T. Cochrane, G. J. Milburn, and W. J. Munro, Macroscopically distinct quantum-superposition states as a bosonic code for amplitude damping, Phys. Rev. A **59**, 2631 (1999).
[27] M. Mirrahimi, Z. Leghtas, V. V. Albert, S. Touzard, R. J. Schoelkopf, L. Jiang, and M. H. Devoret, Dynamically protected cat-qubits: a new paradigm for universal quantum computation, New J. Phys. **16**, 045014 (2014).
[28] A. L. Grimsmo, J. Combes, and B. Q. Baragiola, Quantum Computing with Rotation-Symmetric Bosonic Codes, Phys. Rev. X **10**, 011058 (2020).
[29] I. L. Chuang and Y. Yamamoto, Simple quantum computer, Phys. Rev. A **52**, 3489 (1995).
[30] J. D. Teoh, P. Winkel, H. K. Babla, B. J. Chapman, J. Claes, S. J. de Graaf, J. W. Garmon, W. D. Kalfus, Y. Lu, A. Maiti, K. Sahay, N. Thakur, T. Tsunoda, S. Xue, L. Frunzio, S. M. Girvin, S. Puri, and R. J. Schoelkopf, Dual-rail encoding with superconducting cavities, (2022), ArXiv:quant-ph/2212.12077.
[31] Y. Y. Gao, B. J. Lester, K. S. Chou, L. Frunzio, M. H. Devoret, L. Jiang, S. M. Girvin, and R. J. Schoelkopf, Entanglement of bosonic modes through an engineered exchange interaction, Nature **566**, 509 (2019).
[32] W.-L. Ma, M. Zhang, Y. Wong, K. Noh, S. Rosenblum, P. Reinhold, R. J. Schoelkopf, and L. Jiang, Path-Independent Quantum Gates with Noisy Ancilla, Phys. Rev. Lett. **125**, 110503 (2020).
[33] P. Reinhold, S. Rosenblum, W.-L. Ma, L. Frunzio, L. Jiang, and R. J. Schoelkopf, Error-corrected gates on an encoded qubit, Nat. Phys. **16**, 822 (2020).

[34] S. Rosenblum, P. Reinhold, M. Mirrahimi, L. Jiang, L. Frunzio, and R. J. Schoelkopf, Fault-tolerant detection of a quantum error, Science **361**, 266 (2018).
[35] M. Grassl, T. Beth, and T. Pellizzari, Codes for the quantum erasure channel, Phys. Rev. A **56**, 33 (1997).
[36] G. Kirchmair, B. Vlastakis, Z. Leghtas, S. E. Nigg, H. Paik, E. Ginossar, M. Mirrahimi, L. Frunzio, S. M. Girvin, and R. J. Schoelkopf, Observation of quantum state collapse and revival due to the single-photon Kerr effect, Nature **495**, 205 (2013).
[37] A. Blais, A. L. Grimsmo, S. Girvin, and A. Wallraff, Circuit quantum electrodynamics, Rev. Mod. Phys. **93**, 025005 (2021).
[38] S. Rosenblum, Y. Y. Gao, P. Reinhold, C. Wang, C. J. Axline, L. Frunzio, S. M. Girvin, L. Jiang, M. Mirrahimi, M. H. Devoret, and R. J. Schoelkopf, A CNOT gate between multiphoton qubits encoded in two cavities, Nat. Commun. **9**, 652 (2018). number: 1,
[39] Y. Xu, Y. Ma, W. Cai, X. Mu, W. Dai, W. Wang, L. Hu, X. Li, J. Han, H. Wang, Y. Song, Z.-B. Yang, S.-B. Zheng, and L. Sun, Demonstration of Controlled-Phase Gates between Two Error-Correctable Photonic Qubits, Phys. Rev. Lett. **124**, 120501 (2020).
[40] Y. Zhang, B. J. Lester, Y. Y. Gao, L. Jiang, R. J. Schoelkopf, and S. M. Girvin, Engineering bilinear mode coupling in circuit QED: Theory and experiment, Phys. Rev. A **99**, 012314 (2019).
[41] B. J. Chapman, S. J. de Graaf, S. X. Xue, Y. Zhang, J. D. Teoh, J. C. Curtis, T. Tsunoda, A. Eickbusch, A. P. Read, A. Kootandavida, S. Mundhaha, L. Frunzio, M. H. Devoret, S. M. Girvin, and R. J. Schoelkopf, A high on-off ratio beamsplitter interaction for gates on bosonically encoded qubits, (2022), ArXiv:quant-ph/2212.11929.
[42] C. Zhou, P. Lu, M. Praquin, T.-C. Chien, R. Kaufman, X. Cao, M. Xia, R. Mong, W. Pfaff, D. Pekker, and M. Hatridge, A modular quantum computer based on a quantum state router, (2022), ArXiv:quant-ph/2109.06848.
[43] Y. Lu, A. Maiti, J. W. O. Garmon, S. Ganjam, Y. Zhang, J. Claes, L. Frunzio, S. M. Girvin, and R. J. Schoelkopf, High fidelity bosonic swaps with a parity-protected mixer (in prep.), (2022), ArXiv:quant-ph/2303.00959.
[44] A. J. Sirois, M. A. Castellanos-Beltran, M. P. DeFeo, L. Ranzani, F. Lecocq, R. W. Simmonds, J. D. Teufel, and J. Aumentado, Coherent-state storage and retrieval between superconducting cavities using parametric frequency conversion, Appl. Phys. Lett. **106**, 172603 (2015).
[45] C. Rigetti and M. Devoret, Fully microwave-tunable universal gates in superconducting qubits with linear couplings and fixed transition frequencies, Phys. Rev. B **81**, 134507 (2010).
[46] J. Schwinger, *On Angular Momentum*, Tech. Rep. NYO-3071 (institution Harvard Univ., Cambridge, MA (United States); Nuclear Development Associates, Inc. (US), 1952).
[47] Y.-D. Wang and A. A. Clerk, Using dark modes for high-fidelity optomechanical quantum state transfer, New J. Phys. **14**, 105010 (2012).
[48] M. Reck, A. Zeilinger, H. J. Bernstein, and P. Bertani, Experimental Realization of Any Discrete Unitary Operator, Phys. Rev. Lett. **73**, 58 (1994).
[49] J. A. Jones, V. Vedral, A. Ekert, and G. Castagnoli, Geometric quantum computation using nuclear magnetic resonance, Nature **403**, 869 (2000).
[50] P. J. Leek, J. M. Fink, A. Blais, R. Bianchetti, M. Göppl, J. M. Gambetta, D. I. Schuster, L. Frunzio, R. J. Schoelkopf, and A. Wallraff, Observation of Berry's phase in a solid-state qubit, Science **318**, 1889 (2007).
[51] T. Karzig, Y. Oreg, G. Refael, and M. H. Freedman, Universal Geometric Path to a Robust Majorana Magic Gate, Phys. Rev. X **6**, 031019 (2016).
[52] P. W. Shor, Fault-tolerant quantum computation, (1997), ArXiv:quant-ph/9605011.
[53] D. Gottesman and I. L. Chuang, Demonstrating the viability of universal quantum computation using teleportation and single-qubit operations, Nature **402**, 390 (1999).
[54] X. Zhou, D. W. Leung, and I. L. Chuang, Methodology for quantum logic gate construction, Phys. Rev. A **62**, 052316 (2000).
[55] S. Bravyi and A. Kitaev, Universal quantum computation with ideal Clifford gates and noisy ancillas, Phys. Rev. A **71**, 022316 (2005).
[56] M. A. Nielsen and I. L. Chuang, *Quantum Computation and Quantum Information: 10th Anniversary Edition* (Cambridge University Press, 2010).
[57] H.-K. Lau and M. B. Plenio, Universal Quantum Computing with Arbitrary Continuous-Variable Encoding, Phys. Rev. Lett. **117**, 100501 (2016).
[58] R. W. Heeres, B. Vlastakis, E. Holland, S. Krastanov, V. V. Albert, L. Frunzio, L. Jiang, and R. J. Schoelkopf, Cavity State Manipulation Using Photon-Number Selective Phase Gates, Phys. Rev. Lett. **115**, 137002 (2015).
[59] D. Gottesman, A. Kitaev, and J. Preskill, Encoding a qubit in an oscillator, Phys. Rev. A **64**, 012310 (2001).
[60] P. Campagne-Ibarcq, A. Eickbusch, S. Touzard, E. Zalys-Geller, N. E. Frattini, V. V. Sivak, P. Reinhold, S. Puri, S. Shankar, R. J. Schoelkopf, L. Frunzio, M. Mirrahimi, and M. H. Devoret, Quantum error correction of a qubit encoded in grid states of an oscillator, Nature **584**, 368 (2020).
[61] C. Flühmann, T. L. Nguyen, M. Marinelli, V. Negnevitsky, K. Mehta, and J. P. Home, Encoding a qubit in a trapped-ion mechanical oscillator, Nature **566**, 513 (2019).
[62] S. Singh, B. Royer, and S. M. Girvin, Composite pulses in phase space: Measurement-free gate teleportation with hybrid oscillator-qubit systems, APS March Meet. **A67.00009**, (2023).
[63] A. Eickbusch, V. Sivak, A. Z. Ding, S. S. Elder, S. R. Jha, J. Venkatraman, B. Royer, S. M. Girvin, R. J. Schoelkopf, and M. H. Devoret, Fast universal control of an oscillator with weak dispersive coupling to a qubit, Nat. Phys. **18**, 1464 (2022).
[64] H. J. Briegel, D. E. Browne, W. Dür, R. Raussendorf, and M. Van den Nest, Measurement-based quantum computation, Nat. Phys. **5**, 19 (2009).
[65] S. Puri, A. Grimm, P. Campagne-Ibarcq, A. Eickbusch, K. Noh, G. Roberts, L. Jiang, M. Mirrahimi, M. H. Devoret, and S. Girvin, Stabilized Cat in a Driven Nonlinear Cavity: A Fault-Tolerant Error Syndrome Detector, Phys. Rev. X **9**, 041009 (2019).

[66] N. Ofek, A. Petrenko, R. Heeres, P. Reinhold, Z. Leghtas, B. Vlastakis, Y. Liu, L. Frunzio, S. M. Girvin, L. Jiang, M. Mirrahimi, M. H. Devoret, and R. J. Schoelkopf, Extending the lifetime of a quantum bit with error correction in superconducting circuits, Nature **536**, 441 (2016).

[67] M. A. Nielsen, A simple formula for the average gate fidelity of a quantum dynamical operation, Phys. Lett. A **303**, 249 (2002).

[68] J. R. Johansson, P. D. Nation, and F. Nori, QuTiP 2: A Python framework for the dynamics of open quantum systems, Comput. Phys. Commun. **184**, 1234 (2013).

[69] V. V. Sivak, A. Eickbusch, B. Royer, S. Singh, I. Tsioutsios, S. Ganjam, A. Miano, B. L. Brock, A. Z. Ding, L. Frunzio, S. M. Girvin, R. J. Schoelkopf, and M. H. Devoret, Real-time quantum error correction beyond break-even, Nature **616**, 50 (2023).

[70] B. Foxen, *et al.*, (Google AI Quantum), Demonstrating A Continuous Set of Two-Qubit Gates for Near-Term Quantum Algorithms, Phys. Rev. Lett. **125**, 120504 (2020).

[71] Y. Y. Gao, B. J. Lester, Y. Zhang, C. Wang, S. Rosenblum, L. Frunzio, L. Jiang, S. Girvin, and R. J. Schoelkopf, Programmable Interference between Two Microwave Quantum Memories, Phys. Rev. X **8**, 021073 (2018).

[72] P.-Y. Hou, J. J. Wu, S. D. Erickson, D. C. Cole, G. Zarantonello, A. D. Brandt, A. C. Wilson, D. H. Slichter, and D. Leibfried, Coherently coupled mechanical oscillators in the quantum regime, (2022), ArXiv:2205.14841.

[73] L. Ortiz-Gutiérrez, B. Gabrielly, L. F. Muñoz, K. T. Pereira, J. G. Filgueiras, and A. S. Villar, Continuous variables quantum computation over the vibrational modes of a single trapped ion, Opt. Commun. **397**, 166 (2017).

[74] H. Gan, G. Maslennikov, K.-W. Tseng, C. Nguyen, and D. Matsukevich, Hybrid Quantum Computing with Conditional Beam Splitter Gate in Trapped Ion System, Phys. Rev. Lett. **124**, 170502 (2020).

[75] O. Katz and C. Monroe, Programmable quantum simulations of bosonic systems with trapped ions, (2022), ArXiv:2207.13653.

[76] I. D. Kivlichan, J. McClean, N. Wiebe, C. Gidney, A. Aspuru-Guzik, G. K.-L. Chan, and R. Babbush, Quantum Simulation of Electronic Structure with Linear Depth and Connectivity, Phys. Rev. Lett. **120**, 110501 (2018).

[77] Y. Ma, Y. Xu, X. Mu, W. Cai, L. Hu, W. Wang, X. Pan, H. Wang, Y. P. Song, C.-L. Zou, and L. Sun, Error-transparent operations on a logical qubit protected by quantum error correction, Nat. Phys. **16**, 827 (2020).

[78] T. Walter, P. Kurpiers, S. Gasparinetti, P. Magnard, A. Potočnik, Y. Salathé, M. Pechal, M. Mondal, M. Oppliger, C. Eichler, and A. Wallraff, Rapid High-Fidelity Single-Shot Dispersive Readout of Superconducting Qubits, Phys. Rev. Appl. **7**, 054020 (2017).